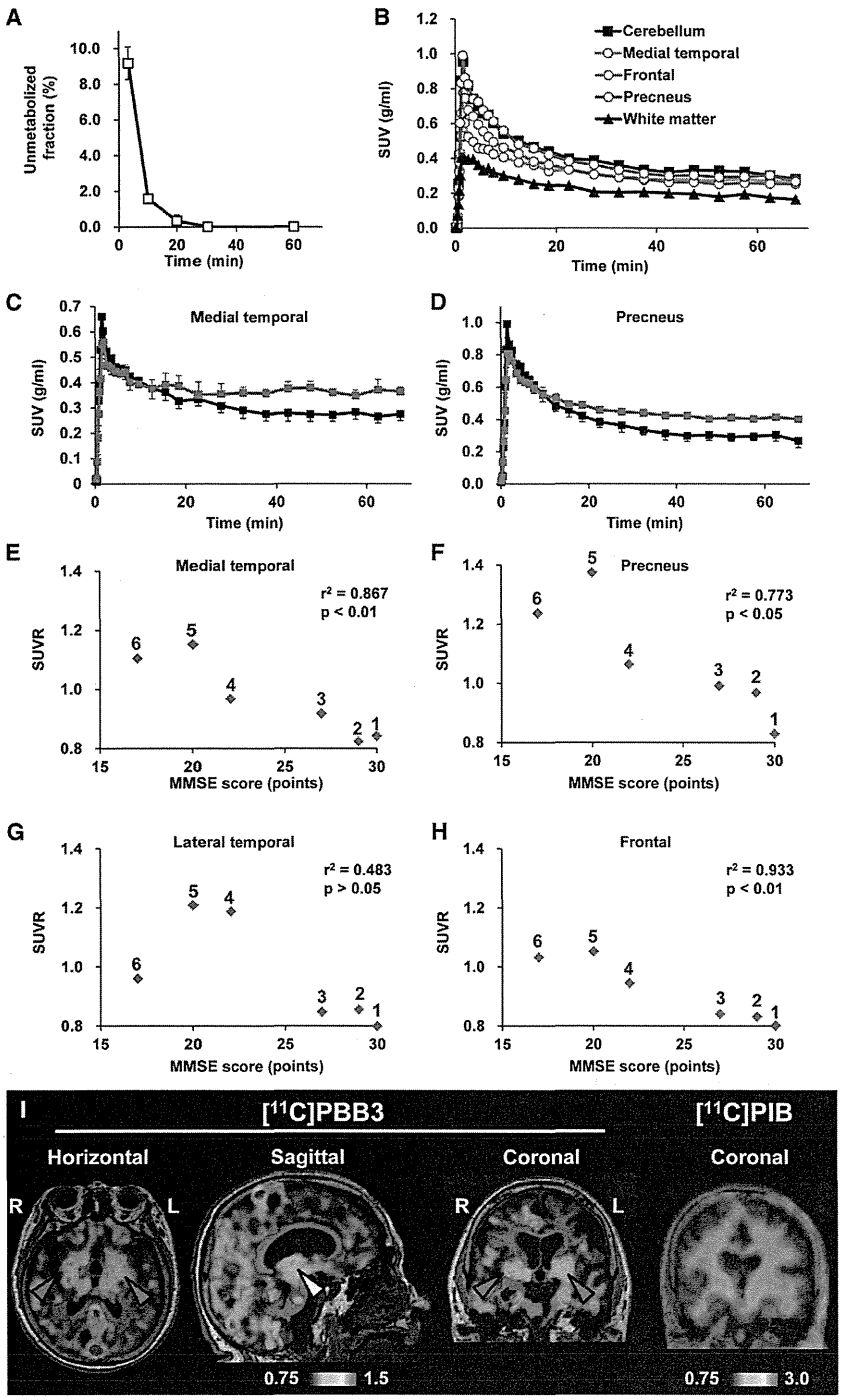

Figure 9. Pharmacokinetic Profiles of [^{11}C]PBB3 Administered to Humans and PET Images of a Patient Clinically Diagnosed as Having Corticobasal Syndrome

(A) Time course of unmetabolized [^{11}C]PBB3 fraction in plasma following intravenous radiotracer injection. The plot was generated by averaging data from six individuals.

(B) Time-radioactivity curves in different brain regions of cognitively normal control subjects over 70 min after intravenous injection of [^{11}C]PBB3. Data were generated by averaging values in two individuals and are presented as standard uptake values (SUVs).

(C and D) Comparisons of time-radioactivity curves in the medial temporal region (C) and precuneus (D) of normal controls (black symbols and lines; n = 3) and AD patients (red symbols and lines; n = 3).

(E–H) Scatterplots illustrating correlation of SUVRs with MMSE scores in the medial temporal region (E), precuneus (F), and lateral temporal (G) and frontal (H) cortices. Numbers beside symbols denote subject ID as indicated in Figure 8. Coefficients of determination (r^2) and p values by t test are displayed in graphs.

(I) [^{11}C]PBB3- and [^{11}C]PIB-PET images in a subject with clinical diagnosis of corticobasal syndrome. Images were generated as in Figures 7 and 8. Accumulation of [^{11}C]PBB3 was noticeable in the basal ganglia (red arrowheads) with right-side dominance and an area containing the thalamus and midbrain (yellow arrowhead).

Vertical bars in the graphs represent SEs. See also Figures S8 and S9.

at a pseudoequilibrium state in human PET imaging (<0.2 nM), [^{11}C]PBB3 is presumed to preferentially bind to tau lesions relative to in vitro autoradiographic (~1 nM) and fluorescence (>100 nM) labeling.

We also estimated contribution of [^{11}C]PBB3 bound to dense core plaques to total radiosignals in the neocortical gray matter of AD patients, by conducting autoradiography and FSB histochemistry for the same sections. Radiolabeling associated with dense cored plaques accounted for less than 1% and 3% of total gray matter signals in the temporal cortex and precuneus, respectively (Figures S9D–S9H). Moreover, fluorescence labeling of adjacent sections with PBB3 demonstrated that approximately 2% and 5% of total gray matter fluorescence signals were attributable to PBB3 bound to dense core plaques in the temporal cortex and precuneus, respectively. Hence, dense cored plaques were conceived to be rather minor sources of binding sites for [^{11}C]PBB3.

Finally, PET scans with [^{11}C]PBB3 and [^{11}C]PIB were conducted for a subject clinically diagnosed as having corticobasal syndrome. Retention of [^{11}C]PIB stayed at a control level, but notable accumulation of [^{11}C]PBB3 was observed in the neocortex and subcortical structures (Figure 9I), providing evidence for in vivo detection of tau lesions in plaque-negative

tauopathies. Interestingly, right-side dominant [^{11}C]PBB3-PET signals in the basal ganglia were consistent with laterality of atrophy in this area (Figure S8F). These findings may also be associated with a right-side dominant decrease in cerebral blood flow and left-side dominant motor signs in this patient.

DISCUSSION

Here, we report our efforts to develop BBB-penetrant ligands that are capable of binding to and visualizing intracellular tau aggregates in AD and non-AD tauopathies. These compounds may accordingly be useful for the differential diagnosis of neurological conditions in elderly subjects on the basis of the distribution of tau lesions, thereby opening up novel avenues for research in elucidating mechanisms of tau-mediated neurodegeneration, as well as tau-focused biomarkers and therapies.

Despite numerous efforts to develop imaging ligands to visualize tau pathologies in the brains of patients with AD and related tauopathies, the urgent need for these tau biomarkers remains largely unmet. To address this significant challenge, we also took advantage of a multimodal imaging system, which facilitates a quick and label-free validation of candidate compounds in terms of their transfer to the brain and retention in tau-rich regions. In addition, subcellular-resolution imaging optics exemplified by two-photon laser scanning microscopy provided proof of the rapid transfer of intravenously administered potential tau pathology imaging agents from plasma to the CNS extracellular matrix and subsequently to the cytoplasm of neurons, where they can bind to intracellular tau inclusions. Based on these encouraging preliminary data using nonlabeled compounds, a subset of these compounds was radiolabeled for use in PET imaging of Tg mice that model tau pathology, and a radioligand that yielded the best visualization of tau lesions in these Tg mice was selected for further testing in human AD patients and NC subjects as well as patients with probable CBD. This stepwise strategy enabled us to identify and advance the most promising PET probe for the visualization and quantitative assessment of tau pathology in the CNS of living human subjects. Interestingly, another research group has recently reported development of ^{18}F-labeled PET ligands for tau lesions mostly through assessments of binding to brain tissues, but not recombinant tau assemblies (Zhang et al., 2012; Chien et al., 2013), as in the present approach. These radioligands have been implied to produce considerably high contrasts for tau pathologies in living AD brains, and relatively long radioactive half-life of ^{18}F would enable delivery of radioligands from a radiosynthesis sites to multiple PET facilities. [^{11}C]PBB3 has distinct advantages over these compounds, as exemplified by affinity for diverse tau lesions, including Tg mouse tau aggregates, applicability to multimodal imaging, and induction of smaller radioactive exposure than ^{18}F-labeled ligands.

In the present work, we clinically validated the performance of [^{11}C]PBB3 as a tau imaging agent by comparing the distribution of [^{11}C]PBB3 with that of [^{11}C]PIB in AD brains. Tau deposits in patients with moderate or severe AD are thought to be distributed extensively in the neocortical and limbic regions (classified as Braak stage V/VI) (Braak and Braak, 1991), thereby resembling localization of senile plaques, except for the predominance of tau aggregates in the hippocampal formation. This rationalizes the use of radioactivity in the medial temporal area as an index to validate an imaging probe for tau pathology versus Aβ deposits in AD patients from prodromal to advanced stages. Furthermore, our preliminary data suggest that [^{11}C]PBB3 may be capable of capturing the temporospatial spreading of neurofibrillary tau pathologies from the limbic system (Braak stage III/IV or earlier) to neocortical areas (Braak stage V/VI) with the progression of AD (Figure 8). A considerable subset of tau lesions at Braak stage I/II is composed of phosphorylated tau deposits barely reactive with thioflavin-S (i.e., pretangles), and NFTs are relatively low in number and are confined to the transentorhinal cortex (Braak and Braak, 1991; Braak et al., 2011). Therefore, detection of these early tau pathologies would be more difficult. Our next-stage clinical study with expanded sample size and wider range of MMSE scores is currently ongoing to pursue tau accumulation in normal controls and subjects with mild cognitive impairments and AD at diverse stages and will bring more compelling insights into the significance of tau PET imaging in early diagnosis and prediction of AD. In addition, alterations of [^{11}C]PBB3 retention were indicated in the transition from mild to moderate AD. Loss of PET signals in the lateral temporal cortex of a patient with moderate AD (subject 6 in Figure 8) might not result from atrophy of this region, as the hippocampus of the same subject exhibited strong [^{11}C]PBB3 binding despite marked atrophy. Possible explanations for this change include formation of extracellular NFTs and their envelopment by astrocytes in the degenerating neocortex, profoundly modifying accessibility of these NFTs to exogenous molecules (Schmidt et al., 1988). This notion would need to be examined by combined autoradiogarphic and immunohistochemical assays of different brain regions.

Being able to visualize tau deposits with [^{11}C]PBB3 in non-AD tauopathies, such as PSP, CBD, and related disorders, is also of major importance, as suggested in the present PET data the support detectability of tau deposition in living CBD brains. As compared with NFTs and neuropil threads in AD, abundant tau deposits are largely confined to specific neuroanatomical locations of the CNS in tau-positive, plaque-negative illnesses, as exemplified by PSP and CBD (Dickson et al., 2011), but the homogenous and low-level background signals of [11C]PBB3 in brain parenchyma indicate the possibility of detecting tau lesions in these disorders. Following such in vivo assessments, a postmortem neuropathological evaluation of scanned subjects would be required as a reference standard for PET assays of non-AD tau pathologies.

[^{11}C]PIB-positive plaque formation nearly plateaus prior to the progression of brain atrophy in AD (Engler et al., 2006), but tau abnormalities may bridge the chasm between Aβ fibrillogenesis and neuronal death. Consistent with this notion, our PET/MRI data indicate that the deposition of tau inclusions as visualized by the intense [^{11}C]PBB3 labeling but lacking overt [^{11}C]PIB binding is closely associated with a local volume reduction in the hippocampal formation. Indeed, our pilot clinical PET study demonstrated that localized accumulation of [^{11}C]PBB3 in the medial temporal region of AD patients was accompanied by marked hippocampal atrophy (Figure 7B). Notably, [^{11}C]PBB3-PET signals were substantially increased, notwithstanding the atrophy-related partial volume effects on PET images, and this

observation may support the contribution of tau fibrils to toxic neuronal death in AD. However, these data do not immediately imply neurotoxicities of [^{11}C]PBB3-reactive tau fibrils, in light of MRI-detectable neurodegeneration uncoupled with [^{11}C]PBB3 retention in the hippocampus of PS19 mice. In the hippocampal formation of AD patients, neurons bearing NFTs that resemble those in the PS19 hippocampus may drive neurodegeneration similar to that observed in either the PS19 hippocampus or brain stem, and this issue could be addressed in future studies using [^{11}C]PBB3-PET and MRI in diverse mouse models, including PS19 and rTg4510 mice, and human subjects.

Our analyses of multiple β sheet ligands illustrated electrochemical and/or conformational diversities of β-pleated sheets among amyloid aggregates, producing a selectivity of these compounds for a certain spectrum of fibrillar pathologies (Figures 1 and S1). Lipophilicities of the β sheet ligands could determine their reactivity with noncored plaques, as noted among the PBBs studied here (Figure 1), although the molecular properties underlying this variation are yet to be elucidated. Meanwhile, we noted that all β sheet ligands tested in the present study were reactive with dense core plaques regardless of their lipophilicities. This may affect in vivo PET signals, particularly in AD brain areas with abundant cored plaques, such as the precuneus. However, our combined autoradiographic and histochemical assessments indicated that [^{11}C]PBB3 bound to dense core plaques accounts for less than 10% of total specific radioligand binding in these areas, and this percentage in fact includes binding to tau fibrils in plaque neurites in addition to Aβ amyloid core. A second possibility to account for the diversity of ligand reactivity to tau lesions may arise from the packing distance between two juxtaposed β sheets in tau filaments and is discussed in the Supplemental Discussion.

Notably, selectivity of [^{11}C]PBB3 for tau versus aggregates may depend on free radioligand concentration in the brain. Our autoradiographic binding assays suggested that affinity of [^{11}C]PBB3 for NFTs is 40- to 50-fold higher than senile plaques, but binding components on tau fibrils may be more readily saturated by this radioligand than those on Aβ fibrils. [^{11}C]PBB3-PET data in humans indicated that uptake of this radioligand into the brain is less than one-third of [^{11}C]PIB uptake and that free radioligand concentration in the brain at a pseudoequilibrium state is approximately 0.2 nM or lower. In this range of concentration, [^{11}C]PBB3 could preferentially interact with high-affinity binding components formed by tau assemblies. An excessive amount of radioligand in the brain would result in saturation of radioligand binding to tau lesions and increased binding to low-affinity, high-capacity binding components in Aβ plaques, and such overload of free radioligand is more likely in regions with less abundant tau pathologies. This could be even more critical in capturing early tau pathologies that originate in the hippocampal formation and may require technical improvements and methodological refinements, including high-resolution imaging, correction for motions of subjects during scans, and robust definition of VOIs on the atrophic hippocampus.

Although nonspecific [^{11}C]PBB3-PET signals in control human subjects were generally low, radioligand retention in dural venous sinuses was noticeable in all scanned individuals. Possible mechanisms that underlie this property are discussed in the Supplemental Discussion.

The present work has also implied the potential utility of multimodal imaging systems for translational development of therapeutic agents that counteract tau fibrillogenesis. Optical imaging with a near-infrared fluorescent probe, such as PBB5, could provide the least invasive technique to assess tau accumulation in living mouse models. As demonstrated by our in vitro and ex vivo fluorescence labeling, all PBBs share a similarity in terms of their reactivity with tau aggregates. Hence, PBB5 optics may be applicable to early screening of therapeutic agents that suppress tau deposition, and the data on abundance of tau lesions obtained by this approach may be translatable to advanced stages of assessments using [^{11}C]PBB3-PET in animal models and humans. By contrast, pharmacokinetic properties of PBB5 (Figure S5) were found to be distinct from those of electrically neutral PBBs, including PBB2 and PBB3. These considerations would be of importance in developing and using fluorescent ligands applicable to optical and PET imaging.

To conclude, our class of multimodal imaging agents offers the possibility of visual investigations of fibrillary tau pathologies at subcellular, cellular, and regional levels. These assay systems are potentially powerful tools for the longitudinal evaluation of anti-tau treatments (Marx, 2007), as a single probe may facilitate a seamless, bidirectional translation between preclinical and clinical insights. PET tracers would also serve a more immediate therapeutic purpose by enabling the assessment of the effects of anti-Aβ and anti-tau therapies on tau pathologies in living AD patients.

EXPERIMENTAL PROCEDURES

Compounds and Reagents

PBB1 (Wako Pure Chemical Industries), PBB2 (ABX), PBB3 (Nard Institute), PBB4 (ABX), mPBB5 (Nard Institute), desmethyl precursor of [^{11}C]PBB2 (2-[4-(4-aminophenyl)buta-1,3-dienyl]benzothiazol-6-ol; Nard Institute), desmethyl precursor of [^{11}C]PBB3 protected with a silyl group (5-[4-(6-tert-butyldimethylsilyloxy-benzothiazol-2-yl)buta-1,3-dienyl]pyridine-2-amine; Nard Institute), desmethyl precursor of [^{11}C]mPBB5 (2-[4-(4-dimethylaminophenyl) buta-1,3-dienyl]-3-ethyl-6-hydroxybenzothiazol-3-ium; Nard Institute), and 2-[8-(4-dimethylaminophenyl)octa-1,3,5,7-tetraenyl]-3-ethylbenzothiazol-3-ium (DM-POTEB; Nard Institute) were custom synthesized. Information on other chemicals is provided in the Supplemental Experimental Procedures. ClogP for each compound was calculated using ACD Chemsketch logP software (Advanced Chemistry Development).

Animal Models

Tg mice heterozygous for human T34 (4-repeat tau isoform with 1 N-terminal insert) with FTDP-17 P301S mutation driven by mouse prion protein promoter, also referred to as PS19 mice (Yoshiyama et al., 2007), were bred and kept on a C57BL/6 background. All mice studied here were maintained and handled in accordance with the National Research Council's Guide for the Care and Use of Laboratory Animals and our institutional guidelines. Protocols for the present animal experiments were approved by the Animal Ethics Committees of the National Institute of Radiological Sciences.

Postmortem Brain Tissues

Procedures for preparation of human and mouse brain sections are given in the Supplemental Experimental Procedures.

In Vitro and Ex Vivo Fluorescence Microscopy

Six micrometer paraffin sections generated from patient brains and 20 μm frozen sections of mouse brains were stained with 10^{-3}% β sheet ligands

dissolved in 50% ethanol for 1 hr at room temperature. Images of the fluorescence signals from these compounds were captured by nonlaser (BZ-9000; Keyence Japan) and confocal laser scanning (FV-1000; Olympus) microscopes. In the confocal imaging, excitation/emission wavelengths (nm) were optimized for each compound as follows: 405/420-520 (PBB3, FSB, PIB, BF-227, BF-158, FDDNP, thioflavin-S), 488/520-580 (PBB2, PBB4), 515/530-630 (PBB1, curcumin), and 635/645-720 (PBB5, BF-189, DM-POTEB). Subsequently, the tested samples and adjacent sections probed serially with each ligand were autoclaved for antigen retrieval, immunostained with the anti-tau monoclonal antibody AT8 that is specific for tau phosphorylated at Ser 202 and Thr 205 (Endogen), as well as a polyclonal antibody against AβN3(pE), and inspected using the microscopes noted above. For ex vivo imaging, PS19 and non-Tg WT at 10–12 months of age were anesthetized with 1.5% (v/v) isoflurane and were given 1 mg/kg PBB1-4, 0.1 mg/kg PBB5, or 10 mg/kg FSB by syringe via tail vein. The animals were killed by decapitation at 60 min after tracer administration. Brain and spinal cord were harvested and cut into 10-μm-thick sections on a cryostat (HM560). The sections were imaged using microscopes as in the in vitro assays and were labeled with either FSB or AT8, followed by microscopic re-examination.

Ex Vivo and In Vivo Multiphoton Imaging

Experimental procedures are given in the Supplemental Experimental Procedures.

In Vivo and Ex Vivo Pulsed Laser Scanning Imaging

Noninvasive scans of isoflurane-anesthetized non-Tg WT and tau Tg mice at 12 months of age were performed using a small animal-dedicated optical imager (eXplore Optix; ART). Scan protocols are given in the Supplemental Experimental Procedures.

Radiosynthesis of [^{11}C]PBB2

Experimental procedures are given in the Supplemental Experimental Procedures.

Radiosynthesis of [^{11}C]PBB3

[^{11}C]Methyl iodide was produced and transferred into 300 μl of dimethyl sulphoxide (DMSO) containing 1.5–2 mg of *tert*-butyldimethylsilyl desmethyl precursor and 10 mg of potassium hydroxide at room temperature. The reaction mixture was heated to 125°C and maintained for 5 min. After cooling the reaction vessel, 5 mg of *tetra-n*-butylammonium fluoride hydrate in 600 μl of water was added to the mixture to delete the protecting group, and then 500 μl of HPLC solvent was added to the reaction vessel. The radioactive mixture was transferred into a reservoir for HPLC purification (CAPCELL PAK C_{18} column, 10 × 250 mm; acetonitrile/50 mM ammonium formate = 4/6, 6 ml/min). The fraction corresponding to [^{11}C]PBB3 was collected in a flask containing 100 μl of 25% ascorbic acid solution and 75 μl of Tween 80 in 300 μl of ethanol and was evaporated to dryness under a vacuum. The residue was dissolved in 10 ml of saline (pH 7.4) to obtain [^{11}C]PBB3 (970–1,990 GBq at the end of synthesis [EOS]) as an injectable solution. The final formulated product was radiochemically pure (≥95%) as detected by analytic HPLC (CAPCELL PAK C_{18} column, 4.6 × 250 mm; acetonitrile/50 mM ammonium formate = 4/6, 2 ml/min). The specific activity of [^{11}C]PBB3 at EOS was 37–121 GBq/μmol, and [^{11}C]PBB3 maintained its radioactive purity exceeding 90% over 3 hr after formulation.

Radiosynthesis of [^{11}C]mPBB5

Experimental procedures are given as Supplemental Experimental Procedures.

Radiosynthesis of [^{11}C]PIB

Radiolabeling of PIB was performed as described elsewhere (Maeda et al., 2011). The specific activity of [^{11}C]PIB at EOS was 50–110 GBq/μmol.

In Vitro and Ex Vivo Autoradiography

Experimental procedures are given in the Supplemental Experimental Procedures.

In Vivo PET Imaging of Mice

PET scans were performed using a microPET Focus 220 animal scanner (Siemens Medical Solutions) immediately after intravenous injection of [^{11}C]PBB2 (28.3 ± 10.3 MBq), [^{11}C]PBB3 (29.7 ± 9.3 MBq), or [^{11}C]mPBB5 (32.8 ± 5.9 MBq). Detailed procedures are provided in the Supplemental Experimental Procedures.

In Vivo PET Imaging of Humans

Three cognitively normal control subjects (64, 72, and 75 years of age; mean age, 70.3 years) and three AD patients (64, 75 and 77 years of age; mean age, 72 years) were recruited to the present work (Figure 8). Additional information on these subjects is given in the Supplemental Experimental Procedures. The current clinical study was approved by the Ethics and Radiation Safety Committees of the National Institute of Radiological Sciences. Written informed consent was obtained from the subjects or their family members. PET assays were conducted with a Siemens ECAT EXACT HR+ scanner (CTI PET Systems). Detailed PET scan protocols are provided in the Supplemental Experimental Procedures. A fraction of radioactivity corresponding to unmetabolized [^{11}C]PBB3 in plasma at 3, 10, 20, 30, and 60 min was determined by HPLC (Waters mBondapak C_{18} column, 7.8 × 300 mm; acetonitrile/ammonium formate mobile phase with gradient elution = 40/60, 52/48, 80/20, 80/20, 40/60, and 40/60 at 0, 6, 7, 8, 9, and 15 min, respectively; flow rate, 6 ml/min) as described elsewhere (Suzuki et al., 1999). The radiotracer injection and following scans and plasma assays were conducted in a dimly lit condition to avoid photoracemization of the chemicals.

Individual MRI data were coregistered to the PET images using PMOD software (PMOD Technologies). Volumes of interest (VOIs) were drawn on coregistered MR images and were transferred to the PET images. Procedures of image analyses are provided in the Supplemental Experimental Procedures.

We additionally carried out PET scans of a patient who was clinically diagnosed as having corticobasal syndrome, as described in the Supplemental Experimental Procedures.

SUPPLEMENTAL INFORMATION

Supplemental Information includes Supplemental Experimental Procedures, nine figures, and one table and can be found with this article online at http://dx.doi.org/10.1016/j.neuron.2013.07.037.

ACKNOWLEDGMENTS

The authors thank Mr. T. Minamihisamatsu and Mr. Y. Matsuba for technical assistance, the staff of the Molecular Probe Group, National Institute of Radiological Sciences, for support with radiosynthesis, Dr. Y. Yoshiyama at National Hospital Organization Chiba-East Hospital for his support on clinical PET studies, and Dr. T. Iwatsubo at the University of Tokyo and Dr. H. Inoue at Kyoto University for their critical discussions. This work was supported in part by grants from the National Institute on Aging of the National Institutes of Health (AG10124 and AG17586) (to J.Q.T. and V. M.-Y.L.), Grants-in-Aid for Japan Advanced Molecular Imaging Program, Young Scientists (21791158) (to M.M.), Scientific Research (B) (23390235) (to M.H.), Core Research for Evolutional Science and Technology (to T.S.), Scientific Research on Innovative Areas ("Brain Environment") (23111009) (to M.H.) from the Ministry of Education, Culture, Sports, Science and Technology, Japan, Thomas H. Maren Junior Investigator Fund from College of Medicine, University of Florida (to N.S.), and research fund of Belfer Neurodegeneration Consortium (to Q.C. and M.-K.J.). M.M., H. Shimada, T.S., M.-R.Z., and M.H. are named as inventors on a patent application 0749006WO1, claiming subject matter related to the results described in this paper.

Accepted: July 12, 2013
Published: September 18, 2013

REFERENCES

Bacskai, B.J., Hickey, G.A., Skoch, J., Kajdasz, S.T., Wang, Y., Huang, G.F., Mathis, C.A., Klunk, W.E., and Hyman, B.T. (2003). Four-dimensional

multiphoton imaging of brain entry, amyloid binding, and clearance of an amyloid-β ligand in transgenic mice. Proc. Natl. Acad. Sci. USA *100*, 12462–12467.

Ballatore, C., Lee, V.M.Y., and Trojanowski, J.Q. (2007). Tau-mediated neurodegeneration in Alzheimer's disease and related disorders. Nat. Rev. Neurosci. *8*, 663–672.

Braak, H., and Braak, E. (1991). Neuropathological stageing of Alzheimer-related changes. Acta Neuropathol. *82*, 239–259.

Braak, H., Thal, D.R., Ghebremedhin, E., and Del Tredici, K. (2011). Stages of the pathologic process in Alzheimer disease: age categories from 1 to 100 years. J. Neuropathol. Exp. Neurol. *70*, 960–969.

Chien, D.T., Bahri, S., Szardenings, A.K., Walsh, J.C., Mu, F., Su, M.Y., Shankle, W.R., Elizarov, A., and Kolb, H.C. (2013). Early clinical PET imaging results with the novel PHF-tau radioligand [F-18]-T807. J. Alzheimers Dis. *34*, 457–468.

Dickson, D.W., Kouri, N., Murray, M.E., and Josephs, K.A. (2011). Neuropathology of frontotemporal lobar degeneration-tau (FTLD-tau). J. Mol. Neurosci. *45*, 384–389.

Engler, H., Forsberg, A., Almkvist, O., Blomquist, G., Larsson, E., Savitcheva, I., Wall, A., Ringheim, A., Långström, B., and Nordberg, A. (2006). Two-year follow-up of amyloid deposition in patients with Alzheimer's disease. Brain *129*, 2856–2866.

Fodero-Tavoletti, M.T., Okamura, N., Furumoto, S., Mulligan, R.S., Connor, A.R., McLean, C.A., Cao, D., Rigopoulos, A., Cartwright, G.A., O'Keefe, G., et al. (2011). ^{18}F-THK523: a novel *in vivo* tau imaging ligand for Alzheimer's disease. Brain *134*, 1089–1100.

Higuchi, M., Iwata, N., Matsuba, Y., Sato, K., Sasamoto, K., and Saido, T.C. (2005). ^{19}F and ^{1}H MRI detection of amyloid β plaques *in vivo*. Nat. Neurosci. *8*, 527–533.

Hintersteiner, M., Enz, A., Frey, P., Jaton, A.L., Kinzy, W., Kneuer, R., Neumann, U., Rudin, M., Staufenbiel, M., Stoeckli, M., et al. (2005). *In vivo* detection of amyloid-β deposits by near-infrared imaging using an oxazine-derivative probe. Nat. Biotechnol. *23*, 577–583.

Klunk, W.E., Wang, Y., Huang, G.F., Debnath, M.L., Holt, D.P., Shao, L., Hamilton, R.L., Ikonomovic, M.D., DeKosky, S.T., and Mathis, C.A. (2003). The binding of 2-(4′-methylaminophenyl)benzothiazole to postmortem brain homogenates is dominated by the amyloid component. J. Neurosci. *23*, 2086–2092.

Klunk, W.E., Engler, H., Nordberg, A., Wang, Y., Blomqvist, G., Holt, D.P., Bergström, M., Savitcheva, I., Huang, G.F., Estrada, S., et al. (2004). Imaging brain amyloid in Alzheimer's disease with Pittsburgh Compound-B. Ann. Neurol. *55*, 306–319.

Krebs, M.R.H., Bromley, E.H., and Donald, A.M. (2005). The binding of thioflavin-T to amyloid fibrils: localisation and implications. J. Struct. Biol. *149*, 30–37.

Kudo, Y., Okamura, N., Furumoto, S., Tashiro, M., Furukawa, K., Maruyama, M., Itoh, M., Iwata, R., Yanai, K., and Arai, H. (2007). 2-(2-[2-Dimethylaminothiazol-5-yl]ethenyl)-6- (2-[fluoro]ethoxy)benzoxazole: a novel PET agent for *in vivo* detection of dense amyloid plaques in Alzheimer's disease patients. J. Nucl. Med. *48*, 553–561.

Maeda, J., Ji, B., Irie, T., Tomiyama, T., Maruyama, M., Okauchi, T., Staufenbiel, M., Iwata, N., Ono, M., Saido, T.C., et al. (2007). Longitudinal, quantitative assessment of amyloid, neuroinflammation, and anti-amyloid treatment in a living mouse model of Alzheimer's disease enabled by positron emission tomography. J. Neurosci. *27*, 10957–10968.

Maeda, J., Zhang, M.R., Okauchi, T., Ji, B., Ono, M., Hattori, S., Kumata, K., Iwata, N., Saido, T.C., Trojanowski, J.Q., et al. (2011). *In vivo* positron emission tomographic imaging of glial responses to amyloid-beta and tau pathologies in mouse models of Alzheimer's disease and related disorders. J. Neurosci. *31*, 4720–4730.

Marx, J. (2007). Alzheimer's disease. A new take on tau. Science *316*, 1416–1417.

Okamura, N., Suemoto, T., Furumoto, S., Suzuki, M., Shimadzu, H., Akatsu, H., Yamamoto, T., Fujiwara, H., Nemoto, M., Maruyama, M., et al. (2005). Quinoline and benzimidazole derivatives: candidate probes for *in vivo* imaging of tau pathology in Alzheimer's disease. J. Neurosci. *25*, 10857–10862.

Santacruz, K., Lewis, J., Spires, T., Paulson, J., Kotilinek, L., Ingelsson, M., Guimaraes, A., DeTure, M., Ramsden, M., McGowan, E., et al. (2005). Tau suppression in a neurodegenerative mouse model improves memory function. Science *309*, 476–481.

Schmidt, M.L., Gur, R.E., Gur, R.C., and Trojanowski, J.Q. (1988). Intraneuronal and extracellular neurofibrillary tangles exhibit mutually exclusive cytoskeletal antigens. Ann. Neurol. *23*, 184–189.

Small, G.W., Kepe, V., Ercoli, L.M., Siddarth, P., Bookheimer, S.Y., Miller, K.J., Lavretsky, H., Burggren, A.C., Cole, G.M., Vinters, H.V., et al. (2006). PET of brain amyloid and tau in mild cognitive impairment. N. Engl. J. Med. *355*, 2652–2663.

Suzuki, K., Takei, M., and Kida, T. (1999). Development of an analyzing system for the sensitive measurement of radioactive metabolites on the PET study. J. Labelled Comp. Radiopharm. *42*, S658–S660.

Thompson, P.W., Ye, L., Morgenstern, J.L., Sue, L., Beach, T.G., Judd, D.J., Shipley, N.J., Libri, V., and Lockhart, A. (2009). Interaction of the amyloid imaging tracer FDDNP with hallmark Alzheimer's disease pathologies. J. Neurochem. *109*, 623–630.

Yang, L., Rieves, D., and Ganley, C. (2012). Brain amyloid imaging—FDA approval of florbetapir F18 injection. N. Engl. J. Med. *367*, 885–887.

Yoshiyama, Y., Higuchi, M., Zhang, B., Huang, S.M., Iwata, N., Saido, T.C., Maeda, J., Suhara, T., Trojanowski, J.Q., and Lee, V.M.Y. (2007). Synapse loss and microglial activation precede tangles in a P301S tauopathy mouse model. Neuron *53*, 337–351.

Zhang, W., Arteaga, J., Cashion, D.K., Chen, G., Gangadharmath, U., Gomez, L.F., Kasi, D., Lam, C., Liang, Q., Liu, C., et al. (2012). A highly selective and specific PET tracer for imaging of tau pathologies. J. Alzheimers Dis. *31*, 601–612.

Zhuang, Z.P., Kung, M.P., Hou, C., Skovronsky, D.M., Gur, T.L., Plössl, K., Trojanowski, J.Q., Lee, V.M.Y., and Kung, H.F. (2001). Radioiodinated styrylbenzenes and thioflavins as probes for amyloid aggregates. J. Med. Chem. *44*, 1905–1914.

Journal of Biotechnology 167 (2013) 8–15

Contents lists available at SciVerse ScienceDirect

Journal of Biotechnology

journal homepage: www.elsevier.com/locate/jbiotec

Viral protein-coating of magnetic nanoparticles using simian virus 40 VP1

Teruya Enomoto[a,1], Masaaki Kawano[b,1], Hajime Fukuda[a,1], Wataru Sawada[a,1], Takamasa Inoue[a], Kok Chee Haw[a], Yoshinori Kita[a], Satoshi Sakamoto[a], Yuki Yamaguchi[a], Takeshi Imai[c], Mamoru Hatakeyama[d], Shigeyoshi Saito[e], Adarsh Sandhu[f,g], Masanori Matsui[h], Ichio Aoki[e], Hiroshi Handa[a,d,*]

[a] Department of Biological Information, Graduate School of Bioscience and Biotechnology, Tokyo Institute of Technology, 4259 Nagatsuta-cho, Midori-ku, Yokohama City, Kanagawa 226-8501, Japan
[b] Department of Molecular Biology, Faculty of Medicine, Saitama Medical University, 38 Morohongo, Moroyama-cho, Iruma-gun, Saitama 350-0495, Japan
[c] National Institute of Longevity Sciences, 36-3 Gengo, Moriyama-cho, Obu, Aichi 474-8522, Japan
[d] Solutions Research Laboratory, Tokyo Institute of Technology, 4259 Nagatsuta-cho, Midori-ku, Yokohama City, Kanagawa 226-8503, Japan
[e] Molecular Imaging Center, National Institute of Radiological Sciences, 4-9-1 Anagawa, Inage-ku, Chiba City, Chiba 263-8555, Japan
[f] Electronics-Inspired Interdisciplinary Research Institute, Toyohashi University of Technology, 1-1 Hibarigaoka Tempaku-cho, Toyohashi City, Aichi 441-8580, Japan
[g] Department of Electrical Engineering and Electronics, Tokyo Institute of Technology, 2-12-1 O-okayama, Meguro-ku, Tokyo 152-8550, Japan
[h] Department of Microbiology, Faculty of Medicine, Saitama Medical University, 38 Morohongo, Moroyama-cho, Iruma-gun, Saitama 350-0495, Japan

ARTICLE INFO

Article history:
Received 18 January 2013
Received in revised form 4 June 2013
Accepted 7 June 2013
Available online 17 June 2013

Keywords:
Nanoparticle
Viral capsid protein
Diagnostic
Coating
Targeting

ABSTRACT

Artificial beads including magnetite and fluorescence particles are useful to visualize pathologic tissue, such as cancers, from harmless types by magnetic resonance imaging (MRI) or fluorescence imaging. Desirable properties of diagnostic materials include high dispersion in body fluids, and the ability to target specific tissues. Here we report on the development of novel magnetic nanoparticles (MNPs) intended for use as diagnosis and therapy that are coated with viral capsid protein VP1-pentamers of simian virus 40, which are monodispersive in body fluid by conjugating epidermal growth factor (EGF) to VP1. Critically, the coating of MNPs with VP1 facilitated stable dispersion of the MNPs in body fluids. In addition, EGF was conjugated to VP1 coating on MNPs (VP1-MNPs). EGF-conjugated VP1-MNPs were successfully used to target EGF receptor-expressing tumor cells *in vitro*. Thus, using viral capsid protein VP1 as a coating material would be useful for medical diagnosis and therapy.

1. Introduction

Simian virus 40 (SV40) is a small non-enveloped DNA virus of the *Polyomaviridae* family. The capsid of SV40 is 45 nm in diameter and composed mainly of 72 copies of pentamers of the major capsid protein, VP1 (Liddington et al., 1991). When expressed in insect cells using recombinant baculovirus, VP1 self-assembles into virus-like particles (VLPs) of 45 nm in diameter (Kosukegawa et al., 1996). VLPs isolated from the cells are disassembled *in vitro* into VP1-pentamers by the addition of DTT and EGTA (Ishizu et al., 2001). These VP1-pentamers self-reassemble *in vitro* into 45-nm VLPs under appropriate conditions (Kanesashi et al., 2003; Kawano et al., 2006). During the reassembly, VLPs can encapsulate materials such as DNA (Enomoto et al., 2011; Tsukamoto et al., 2007) and proteins (Inoue et al., 2008). Furthermore, it is possible to confer cell-type specificity to VLPs by inserting foreign peptides (Takahashi et al., 2008) or conjugating human epidermal growth factor (EGF) (Kitai et al., 2011) to VP1. Thus, VP1 of SV40 is potentially very useful as a medical nanomaterial.

Magnetic nanoparticles (MNPs) mainly composed of iron oxide or gadolinium have been developed as MRI contrast agents—materials that reduce the relaxation time of protons (Weinmann et al., 2003). We have previously prepared and reported on the properties of size-controlled and water-dispersed citrate-coated MNPs (CMNPs) (Hatakeyama et al., 2011). Due to their monodispersity in water, we expected that the CMNPs would be suitable as an MRI contrast agent (Hatakeyama et al., 2011). However, CMNPs form aggregates in a physiological salt condition (this study). In addition to dispersibility, the targeted delivery

* Corresponding author at: Graduate School of Bioscience and Biotechnology, Tokyo Institute of Technology, 4259 Nagatsuta-cho, Midori-ku, Yokohama City, Kanagawa 226-8501, Japan. Tel.: +81 45 924 5872; fax: +81 45 924 5834.
E-mail address: hhanda@bio.titech.ac.jp (H. Handa).
[1] These authors contributed equally to this paper.

0168-1656/$ – see front matter © 2013 Elsevier B.V. All rights reserved.
http://dx.doi.org/10.1016/j.jbiotec.2013.06.005

and retention of nanoparticles to specific tissues is an important requirement for the development of MRI contrast agents for diagnosis. Since early MRI contrast agents diffuse well into intravascular and interstitial spaces, there is increasing demand for an agent with a tissue-specific diffusion distribution to improve diagnostic accuracy (Weinmann et al., 2003). In particular, the development of an agent that accumulates highly and specifically in malignant tumors is of interest for clinicians because this may allow an accurate diagnosis in early stages of the disease. To this aim, recently various types of MNPs, such as labeled with tumor-specific monoclonal antibody (Anderson et al., 2000; Gohr-Rosenthal et al., 1993; Remsen et al., 1996; Shahbazi-Gahrouei et al., 2001; Sipkins et al., 1998; Suwa et al., 1998) or presented tumor-selective peptide (Montet et al., 2006; Nasongkla et al., 2006; Uchida et al., 2006), have been synthesized.

Here, we present the synthesis of novel CMNPs that were coated with VP1-pentamers of simian virus 40, which produced CMNPs that were highly dispersive, and that attached at targeted cells by conjugating EGF to VP1. VP1 coating allowed stable dispersion of CMNPs and prevented their aggregation. EGF conjugation to VP1 enabled the selective targeting of the particles to EGF receptor (EGFR) on the cells *in vitro*, which is overexpressed in a variety of tumors (Normanno et al., 2003; Salomon et al., 1995). Thus, highly dispersible CMNPs with cell-targeting ability would be applicable for the diagnosis of tumors by MRI.

2. Materials and methods

2.1. Preparation of VP1 pentamers

$VLPs^{WT}$ and $VLPs^{N138C}$ were prepared as described previously (Ishizu et al., 2001). Briefly, recombinant baculovirus expressing either $VLPs^{WT}$ or $VLPs^{N138C}$ was generated using the baculovirus expressing system (Invitrogen) and Sf-9 cells were infected with these viruses. $VLPs^{WT}$ and $VLPs^{N138C}$ were purified from lysates of virus-infected Sf-9 cells by cesium chloride density gradient and dialyzed in dialysis buffer containing 20 mM Tris–HCl (pH 7.9), 150 mM NaCl and 0.1% NP-40. Purified $VLPs^{WT}$ and $VLPs^{N138C}$ were dissociated in buffer containing 5 mM DTT and 5 mM EGTA, and the dissociated samples were fractionated by gel filtration (Superdex 200, GE Healthcare) to collect homogeneous $VP1^{WT}$- and $VP1^{N138C}$-pentamers. For preparation of $VP1^{\Delta C58}$-pentamers, the C-terminal 58 amino-acids were deleted from VP1 and the histidine tag sequence was fused to the C-terminus of $VP1^{\Delta C58}$. Sf-9 cells were then infected with recombinant baculovirus expressing $VP1^{\Delta C58}$. $VP1^{\Delta C58}$-pentamers were purified from cell lysates by nickel-nitrilotriacetic acid agarose resin (Qiagen) according to the manufacture's instruction. $VP1^{\Delta C58}$-pentamers were further purified by Superose 6 chromatography (GE Healthcare), and then gel fractionation.

2.2. Construction of VP1-CMNPs

CMNPs were prepared as described before (Hatakeyama et al., 2011). CMNPs were mixed with either $VP1^{WT}$-pentamers, $VP1^{N138C}$-pentamers or $VP1^{\Delta C58}$-pentamers at a molar ratio of 1:72. The mixture was dialyzed in coating buffer containing 20 mM MOPS-NaOH (pH 7.0), 150 mM NaCl, and 2 mM $CaCl_2$. To remove free pentamers, the sample was centrifuged at 20,400 × *g* for 15 min at 4 °C. The pellet fraction containing VP1-CMNPs was washed twice and resuspended in coating buffer. For TEM observation, the samples were negatively stained with 2% ammonium molybdate and were observed using a TEM (H-7500, Hitachi) as described previously (Ishizu et al., 2001). The molar of CMNPs was calculated from the Fe^{2+} concentrations in CMNPs suspension and the molecular weight of CMNPs which was estimated from the diameter of its.

2.3. Measurement of diameter and electric potential of nanoparticles

Diameters and zeta potentials of intact CMNPs and $VP1^{WT}$-CMNPs in various solutions were analyzed using Zeta-potential & Particle size Analyzer (ELSZ-2, Otsuka Electronics Co. Ltd., Osaka, Japan) according to the manufacture's protocol.

2.4. Relaxivities and T1- and T2-weighted MR images of VP1-CMNPs

The longitudinal and transverse relaxation times of the different sized CMNPs or VP1-CMNPs were measured in distilled water using a 0.47 T NMR Analyzer (NMS 120 Minispec, Bruker Optics, Ibaraki, Japan) at 40 °C. The longitudinal (r_1) and transverse (r_2) relaxivities of Fe were calculated from the measured relaxation times. The T1- and T2-weighted MR images of freucarbotran, gadopentetate dimeglumine, or 27 nm VP1-CMNPs were obtained using a 7-T horizontal MRI (Biospec, Avence-I, Bruker BioSpin, Germany) with a volume coil for transmission and reception (35 mm inner-diameter, Rapid Biomedical, Germany). Measurement parameters were as follows: spin echo sequence, TR/TE = 400.0/9.6 ms (T1-weighted imaging), or multi-echo spin echo sequence, TR/TE = 3000/60 ms (T2-weighted imaging), field-of-view = 38.4 × 38.4 mm^2, slice thickness = 2 mm, and matrix size = 256 × 256.

2.5. Sucrose gradient sedimentation analysis

Sucrose gradient sedimentation analyses were performed as described previously (Kawano et al., 2006). In brief, 20 μL of samples containing $VP1^{WT}$-CMNPs or $VP1^{\Delta C58}$-CMNPs were loaded onto the top of 600 μL of 20–40% sucrose gradient in 20 mM Tris–HCl (pH 7.9) in a 5 × 41-mm open-top tube and were centrifuged at 232,000 × *g* for 1 h at 4 °C in an SW55Ti rotor (Beckman). After centrifugation, 12 fractions were collected from the top of the gradient. Each fraction was separated by 10% SDS-PAGE, and was analyzed by Western blotting with anti-VP1 antibody (Ishizu et al., 2001).

2.6. Measurement of Fe^{2+} concentration in the blood

Mice were anesthetized with 2.0% isoflurane and were administrated *via* the tail vein with 200 μL of CMNPs or $VP1^{WT}$-CMNPs (7.5 mg/mL) in PBS. Fifty microliters of blood was collected from a femoral artery of mice at various time points after administration. Ten microliters of blood samples was mixed with 990 μL of HNO_3, heated in a microwave oven for 1 min, and then subjected to the ICP-OES analyzer, Prodigy ICP (Teledyne Leeman Labs Inc., NH) to measure the concentration of Fe^{2+} using yttrium as a standard.

2.7. EGF conjugation to VP1-CMNPs

Recombinant human EGF (Peprotech) was conjugated onto $VP1^{WT}$-CMNPs or $VP1^{N138C}$-CMNPs using the heterobifunctional crosslinker with N-hydroxysuccinimide ester and maleimide groups, $SM(PEG)_2$ (Thermo Scientific) as described before (Kitai et al., 2011). Briefly, EGF was incubated with the $SM(PEG)_2$ crosslinker in reaction buffer containing 20 mM MOPS-NaOH (pH 6.5) and 150 mM NaCl for 2 h at 4 °C. After incubation, EGF was quenched in quenching buffer containing 20 mM MOPS-NaOH (pH 6.5), 150 mM NaCl, and 100 mM ethanolamine for 2 h at 4 °C. To remove excess $SM(PEG)_2$, the reaction mixture was dialyzed in the

reaction buffer for 16 h at 4 °C. Then, the linker-conjugated EGF and VP1-CMNPs were mixed at 1.15–1 weight ratio and were incubated for 12 h at 4 °C. After incubation, to quench the reaction, NaOH was added to the sample at a final concentration of 15 mM. The sample was mounted onto the top of 30% sucrose containing PBS and centrifuged at 230,000 × *g* for 15 min at 4 °C in a Beckman SW55Ti rotor. The pellet fraction containing EGF-conjugated $VP1^{WT}$-CMNPs or $VP1^{N138C}$-CMNPs was resuspended in PBS.

2.8. Cell binding assay

The human epidermoid carcinoma cell line, A431 (Hirabayashi et al., 1999) and the human colon adenocarcinoma cell line, WiDr (Noguchi et al., 1979) were kindly provided by Dr. M. Ueda (Keio University, Tokyo, Japan). A431 or WiDr cells (4×10^5 cells) were incubated with EGF-conjugated $VP1^{WT}$-CMNPs or $VP1^{N138C}$-CMNPs at an amount equivalent to 2 μg of VP1 in the presence or absence of various amounts of free EGF for 1 h at 4 °C in serum-free media. Free EGF was used to compete with EGF-conjugated nanoparticles for binding to the EGFR on the cell surface. Cells were collected, resuspended in SDS loading buffer, and then sonicated. Samples were separated by 10% SDS-PAGE, and Western analysis was performed with anti-VP1 (Ishizu et al., 2001) and anti-actin antibodies. Alternatively, sonicated samples were incubated with 100 μL of 6 N HCl for 30 min at 55 °C, and were then subjected to ICP-OES analyzer, Prodigy ICP (Teledyne Leeman Labs Inc, NH) to measure the Fe^{2+} concentration using yttrium as a standard.

3. Results and discussion

3.1. Synthesis of CMNPs coated with VP1

We have previously reported on the synthesis of water-dispersible CMNPs for use as an MRI contrast agent (Hatakeyama et al., 2011). For use *in vivo*, CMNPs should exhibit stable dispersibility in body fluid. To give the CMNPs an ability of active targeting to cells, here we aimed to synthesize CMNPs encapsulated with SV40-VLPs of 45 nm in diameter. As SV40-VLPs are dispersible *in vivo* and their surfaces can be easily modified by genetic or chemical methods, it led us to expect that encapsulation of CMNPs with SV40-VLPs would also be suitable for active targeting. To evaluate whether the CMNPs were encapsulated in SV40-VLPs, we used CMNPs with diameters of 8, 20, and 27 nm. Firstly, the CMNPs were mixed with wild-type VP1-pentamers ($VP1^{WT}$-pentamers) (the basic subunit of SV40-VLP) in a reaction buffer solution, and the mixtures were then dialyzed against a physiological buffer. Transmission electron microscope (TEM) measurements showed that all of the different-sized CMNPs mixed with $VP1^{WT}$-pentamers were covered with lightly stained layers of 5 nm in thickness (Fig. 1b, lower panels), compared to untreated CMNPs (Fig. 1b, upper panels). These results showed that $VP1^{WT}$-pentamer did not assemble into the 45-nm SV40-VLPs but coated CMNPs with a monolayer of $VP1^{WT}$-pentamer in a CMNP's size-dependent manner. Thus, coating of CMNPs with the $VP1^{WT}$-pentamer occurred instead of encapsulating CMNPs in VLPs. CMNPs coated with $VP1^{WT}$ ($VP1^{WT}$-CMNPs) were monodispersed under physiological salt conditions (Fig. 1b, lower panels), whereas control CMNPs formed aggregates in this buffer (Fig. 1b, upper panels). To further examine the dispersibility of CMNPs, we measured the size distribution of the particles in solution using dynamic light scattering (DLS). The average sizes of $VP1^{WT}$-CMNPs were approximately 10 nm larger than the diameters of original CMNPs (Fig. 1c), confirming that CMNPs of any given size could be coated with $VP1^{WT}$-pentamers. In contrast, the sizes of the control CMNPs in solution were roughly 500 nm, showing uncoated CMNPs to aggregation. Taken together, these findings demonstrated that VP1 coating yielded monodisperse CMNPs under physiological salt conditions.

Table 1
Relaxivities for different sized CMNPs with and without VP1-coating.

Core diameter	8 nm		20 nm		27 nm	
Coating	(−)	VP1	(−)	VP1	(−)	VP1
r_1 (s^{-1} mM^{-1})	30.1	14.8	29.8	16.5	34.3	20.4
r_2 (s^{-1} mM^{-1})	54.7	71.3	268.1	294.3	317.0	238.0
r_2/r_1	1.8	4.8	9.0	17.8	9.2	11.7

To directly examine whether the VP1 coating affected the surface properties of CMNPs, we measured the electric potential of their surfaces (Fig. 1d). Due to the citrate-coating, the surfaces of CMNPs were strongly charged with −18 mV at pH 7. In contrast, the surfaces of $VP1^{WT}$-CMNPs had a weak negative charge of −4 mV, indicating that VP1 coating changed the surface potential of CMNPs. Notably, this finding was supported by experiments showing that the surface potential of VLPs was comparable to that of $VP1^{WT}$-CMNPs.

To characterize the properties of VP1-CMNP as an MRI contrast agent, we measured the relaxivities (r_1, r_2) for different sized (8, 20 and 27 nm) CMNPs with and without VP1-coating in distilled water. The relaxivities of these VP1-CMNPs or CMNPs are shown in Table 1. Generally, at 0.47-T VP1-coating decreased the r_1 of the CMNPs without drastically affecting r_2. The subsequent increase in the r_2/r_1 ratio enhanced the potential of VP1-coated CMNPs as a T2 contrast agent. The r_1 for the 27 nm VP1-CMNPs was similar to that for conventional MRI contrast agents (ferucarbotran, Resovist™, $r_1 = 24.7\ s^{-1}\ mM^{-1}$) and the r_2 was large compared to that of ferucarbotran ($r_2 = 160.0\ s^{-1}\ mM^{-1}$). We also acquired T1- and T2-weighted MR images of 27 nm VP1-CMNPs at 7-T MRI with Gd-DTPA (gadopentetate dimeglumine, Magnevist™) and ferucarbotran (Fig. 1e). The signal intensity for VP1-CMNP in both the T1- and T2-weighted images gradually decreased with the VP1-CMNP concentration. The signal reduction for the VP1-CMNPs was larger than that for ferucarbotran on both T1- and T2-weighted images. From these results it is possible to speculate that VP1-CMNPs have better capability as a T2 contrast agent than conventional ferucarbotran.

The C-terminal region of VP1 is important for pentamer–pentamer interaction between VP1-pentamers during the assembly of SV40-VLPs (Garcea et al., 1987; Yokoyama et al., 2007). Using a VP1 mutant with a 58 amino-acid deletion in the C-terminal region ($VP1^{\Delta C58}$), we investigated whether the pentamer–pentamer interaction would be required for the VP1 coating on the surface of CMNPs. CMNPs were mixed with either $VP1^{WT}$-pentamers or $VP1^{\Delta C58}$-pentamers, and were then examined under the TEM. As shown in Fig. 2a, lightly stained layers 5 nm-thick were around CMNPs regardless of whether the $VP1^{WT}$ or the $VP1^{\Delta C58}$ was used, suggesting that the pentamer–pentamer interaction was not necessary for the attachment of VP1-pentamers onto the surfaces of CMNPs. Unlike $VP1^{WT}$-CMNPs (Fig. 2a, left panel), however, $VP1^{\Delta C58}$-attached CMNPs formed particulate aggregates in physiological buffer solution (Fig. 2a, right panel). We have previously reported that DNA is coated with $VP1^{WT}$-pentamers and therefore promotes the assembly of $VP1^{WT}$-pentamers into 45 nm spherical particles (Tsukamoto et al., 2007). Time-course analysis of this DNA-mediated assembly suggests that $VP1^{WT}$-pentamers form aggregates within the first 1 h of reaction, and then form spherical particles through the interaction between $VP1^{WT}$-pentamers in the next 1 h (Tsukamoto et al., 2007). From this point of view, $VP1^{\Delta C58}$-attached CMNPs lacking the pentamer–pentamer interaction may correspond to $VP1^{WT}$-attached DNA in the early stages of the reaction. To examine the dispersibility of $VP1^{\Delta C58}$-attatched CMNPs under physiological

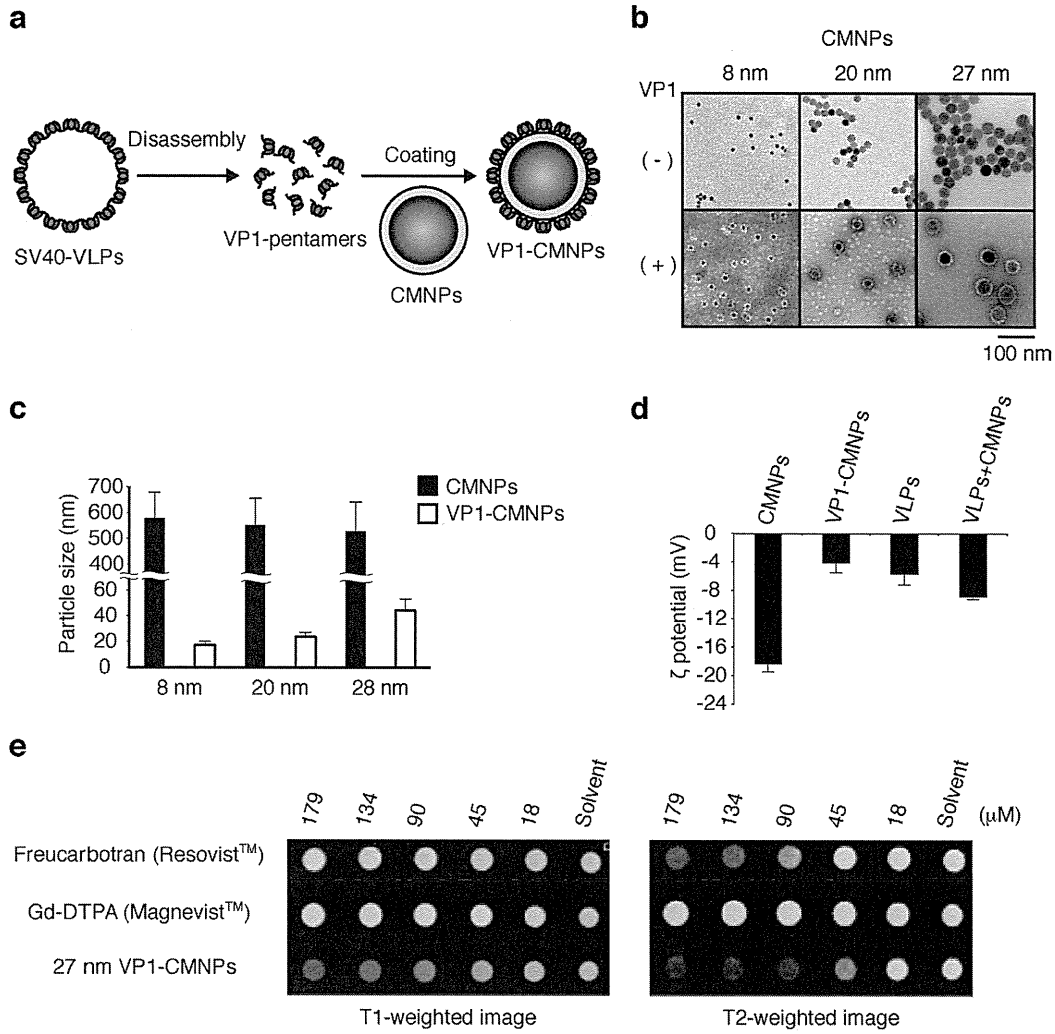

Fig. 1. Synthesis and characterization of VP1-CMNPs. (a) Schematic diagram of the construction of VP1-CMNPs. SV40-VLPs were dissociated into VP1-pentamers. The surfaces of CMNPs were then coated with VP1-pentamers (VP1-CMNPs). (b) Three different-sized CMNPs of 8, 20, and 27 nm in diameter were incubated with (+) or without (−) $VP1^{WT}$-pentamers during dialysis. The samples were visualized by negative staining under the TEM. Scale bar: 100 nm. (c) Diameters of intact CMNPs (black bars) and $VP1^{WT}$-CMNPs (white bars) in the physiological buffer were measured by DSL. Data are shown as the mean ± SD. (d) Zeta-potential of intact CMNPs, $VP1^{WT}$-CMNPs, or SV40-VLPs was analyzed. Data are shown as the mean ± SD. (e) T1-weighted (left) and T2-weighted (right) MR images of MNP (Upper, Ferucarbotran, resovist™), Gd-DTPA and 27 nm VP1-CMNPs at various concentrations. Samples of distilled water were measured as references.

conditions, we carried out sucrose gradient sedimentation analysis (Fig. 2b) (Kawano et al., 2006). After centrifugation, 12 fractions were collected from the top of the gradient. $VP1^{WT}$-CMNPs were found in fractions 5–9 (Fig. 2b, upper panel), whereas $VP1^{\Delta C58}$-attatched CMNPs were detected in the bottom fraction (Fig. 2b, lower panel), suggesting the aggregation of the nanoparticles. These results imply that the pentamer–pentamer interaction is required for the formation of dispersible $VP1^{WT}$-CMNPs.

3.2. Dispersibility of VP1-CMNPs in serum

Practical applications of diagnosis necessitate their dispersibility in body fluids. Therefore, we examined the degree to which $VP1^{WT}$-CMNPs would disperse in serum. $VP1^{WT}$-CMNPs and control CMNPs were incubated in either phosphate buffered saline (PBS) or fetal bovine serum (FBS). In agreement with the data in Fig. 1b and c, $VP1^{WT}$-CMNPs were highly dispersible in PBS, while the control CMNPs aggregated together (Fig. 3a). Surprisingly, $VP1^{WT}$-CMNPs were still dispersible even in FBS (Fig. 3a) although intact CMNPs formed aggregates (Fig. 3a). To verify the TEM results, we measured the diameter of CMNPs. DLS analysis showed that the diameter of $VP1^{WT}$-CMNPs was approximately 40 nm in both PBS and FBS (Fig. 3b), indicating that $VP1^{WT}$-CMNPs were monodispersed in FBS as well as PBS. On the other hand, the control CMNPs in PBS and FBS were 400 and 150 nm in diameter, respectively (Fig. 3b), showing that the water-dispersible, control CMNPs did not disperse in either PBS or FBS. To verify the dispersibility of $VP1^{WT}$-CMNPs *in vivo*, mice were administrated intravenously with an equal dose of CMNPs or $VP1^{WT}$-CMNPs, and the concentration of CMNPs-derived Fe^{2+} in the blood was measured at various times. We expected that highly dispersible $VP1^{WT}$-CMNPs would keep drifting in the blood stream, whereas aggregated CMNPs would tend to settle down and to be quickly uptaken in the liver. As shown in Fig. 3c, the basal Fe^{2+} concentration in both cases was approximately 0.5 mg/μL just before injection. Moreover, we observed rapid increases in Fe^{2+} concentration in both cases just after injection. However, the Fe^{2+} concentration in $VP1^{WT}$-CMNPs-injected mice was approximately twice of that in CMNPs-injected mice at this point in time (Fig. 3c). Furthermore, the Fe^{2+} concentration in both cases gradually decreased to basal level. In addition, the Fe^{2+} concentration decreased much slower in $VP1^{WT}$-CMNPs-injected mice (a half-life of 45 min) than in CMNPs-injected mice (a half-life

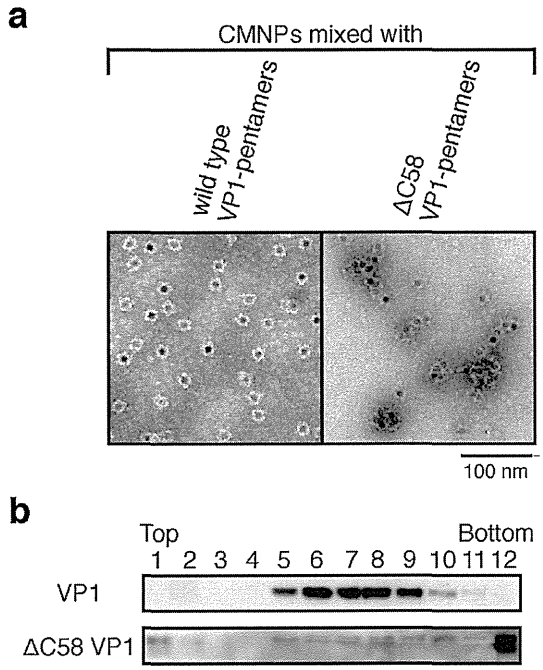

Fig. 2. Requirements of the pentamer–pentamer interaction in the VP1 coating. (a) VP1^{WT}-CMNPs (left panel) and VP1$^{\Delta C58}$-CMNPs (right panel) of 8 nm in diameter were observed under the TEM. Scale bar: 100 nm. (b) Sucrose gradient sedimentation analyses of VP1^{WT}-CMNPs (upper panel) and VP1$^{\Delta C58}$-CMNP (lower panel) of 8 nm in diameter were performed. Fractions were separated by 10% SDS-PAGE and analyzed by Western blot with anti-VP1 antibody. Fractions were numbered from the top to the bottom of the gradient.

of 45 s; Fig. 3c), indicating the longer retention time of VP1^{WT}-CMNPs in blood. These results strongly suggest that VP1^{WT}-CMNPs are dispersive *in vivo*. In this study, the profound liver uptake of aggregated CMNPs might induce quick decline of CMNPs-derived Fe^{2+} concentration in the blood.

3.3. Targeting of EGFR-overexpressing tumor cells by EGF-conjugated VP1-CMNPs

Because EGFR is overexpressed on the surface of various tumor cells (Normanno et al., 2003; Salomon et al., 1995), it is possible to target certain tumor cells through EGFR. We previously constructed SV40-VLPs conjugated with EGF using the heterobifunctional crosslinker, SM(PEG)$_2$ and VP1^{N138C}, in which an asparagine (N) residue located on the outside surface of VLPs (Takahashi et al., 2008) was substituted to a cysteine (C) residue (Kitai et al., 2011). The EGF-conjugated SV40-VLPs were shown to selectively target EGFR-expressing tumor cells *in vitro* (Kitai et al., 2011). Since SM(PEG)$_2$ preferably crosslinks between a primary amine of EGF and the cysteine residue of VLPs^{N138C}, EGF is considered to be selectively attached to the outside surface of VLPs^{N138C}. Moreover, although VP1^{WT} has a partially accessible cysteine residue on the surface of VP1-pentamer, VP1^{N138C} has additional cysteine residue on the surface loop of VP1. It leads us to expect that EGF might be more functionally present on the surface of VP1^{N138C} than VP1^{WT}. In addition, VLPs^{WT} generally bind to a variety of cells through the interaction between the BC, DE, and HI loops of VP1 and GM1 ganglioside on the cells (Takahashi et al., 2008). However, the mutation at position 138 elicits the conformational change of DE loop, and thereby disrupts the binding of EGF-conjugated VLPs^{N138C} to various cells without EGFR expression. Consequently, EGF-conjugated VLPs^{N138C} may be engaged exclusively in EGF-specific targeting.

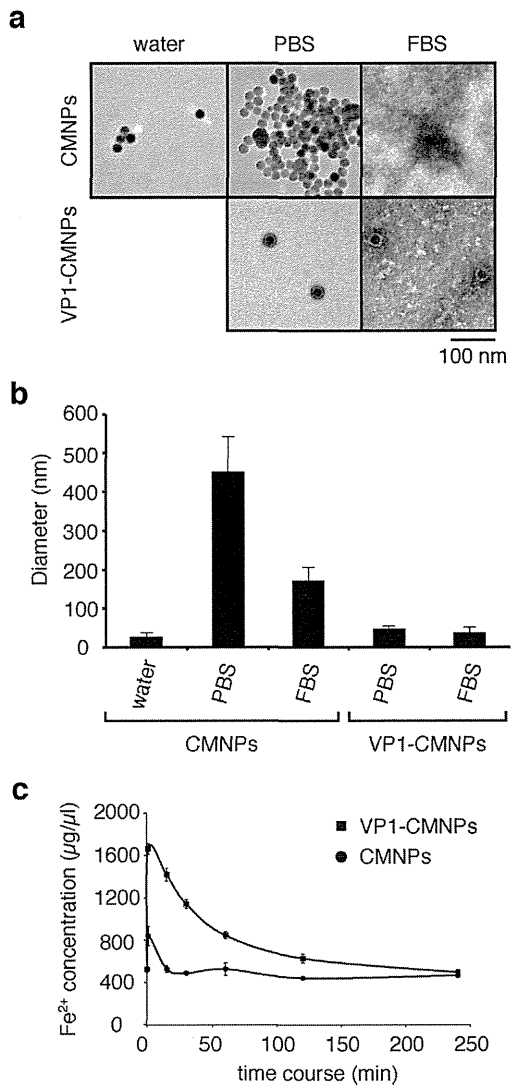

Fig. 3. Dispersibility of VP1-CMNPs *in vitro* and *in vivo*. (a) Intact CMNPs (upper panels) and VP1^{WT}-CMNPs (lower panels) of 27 nm in diameter were incubated in water (left panel), PBS (center panels), or FBS (right panels), and were observed under the TEM. Scale bar: 100 nm. (b) Diameters of intact CMNPs and VP1^{WT}-CMNPs in water, PBS, or FBS were analyzed by DLS. (c) BALB/c mice were injected intravenously with either intact CMNPs or VP1^{WT}-CMNPs of 27 nm in diameter. Blood was collected from each mouse at various time points after injection, and the concentration of Fe^{2+} in the blood was measured by ICP-OES analyzer. Data are shown as the mean ± SD of three samples.

Based on these data (Kitai et al., 2011) and ideas, VP1^{N138C}-coated 27-nm CMNPs (VP1^{N138C}-CMNPs) were synthesized, and EGF conjugated to both VP1^{WT}-CMNPs and VP1^{N138C}-CMNPs using the crosslinker (Fig. 4a). By calculating the intensity of the protein bands from Fig. 4b, the percentage of EGF conjugated to VP1^{N138} protein in total VP1^{N138} protein of VP1^{N138C}-CMNPs appeared to be 26% only slightly larger than that of 18% in VP1^{WT}-CMNPs, suggesting that VP1^{N138C} presents more functionally EGF than VP1^{WT}. VP1^{N138C}-CMNPs were found to be monodispersed in physiological buffer regardless of EGF conjugation (Fig. 4c).

To assess the specificity and efficiency of tumor-targeting by EGF-conjugated VP1^{N138C}-CMNPs, we performed cell binding assay using two human tumor cell lines, A431 (Hirabayashi et al., 1999) and WiDr (Noguchi et al., 1979), which express high and low levels of EGFR, respectively. VP1^{WT}-CMNPs and VP1^{N138C}-CMNPs conjugated with or without EGF were incubated with either A431

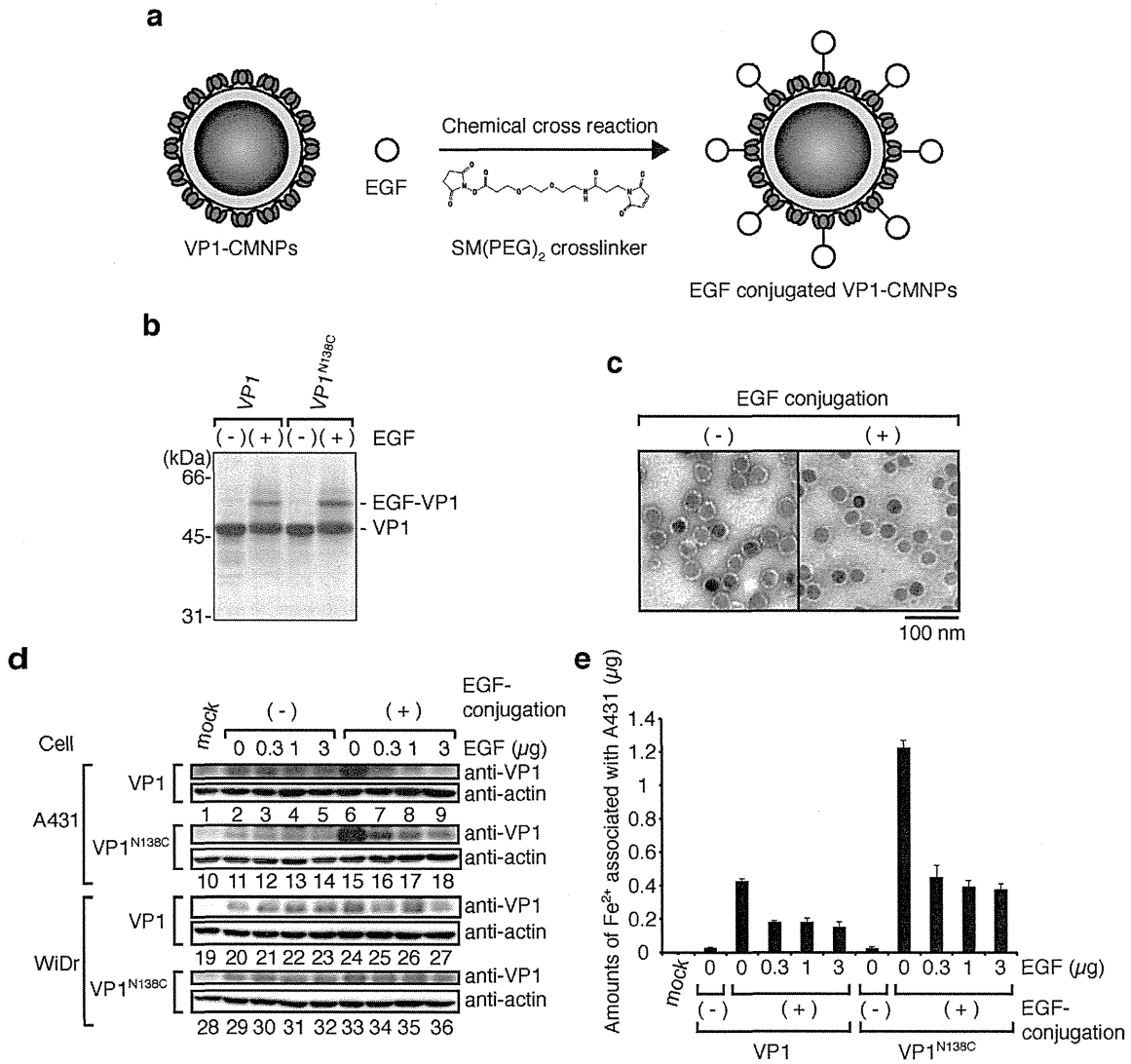

Fig. 4. Targeting of EGFR-overexpressing tumor cells by EGF-conjugated VP1-CMNPs. (a) Schematic diagram of EGF conjugation. EGF was conjugated onto the surface of VP1-CMNPs of 27 nm in diameter using $SM(PEG)_2$ crosslinker. (b) $VP1^{WT}$-CMNPs and $VP1^{N138C}$-CMNPs with (+) or without (-) EGF were loaded onto 10% SDS-PAGE. Positions of EGF conjugated VP1 and free VP1 were indicated. (c) TEM imaging of unconjugated-$VP1^{N138C}$-CMNPs (left panel) and EGF-conjugated $VP1^{N138C}$-CMNPs (right panel). Scale bar: 100 nm. (d) and (e) Cell binding assay. A431 or WiDr cells were incubated with EGF-conjugated either $VP1^{WT}$-CMNPs or $VP1^{N138C}$-CMNPs in the presence or absence of various amounts of free EGF. After incubation, cell lysate were separated by 10% SDS-PAGE, and analyzed by Western blot with anti-VP1 and anti-actin antibodies (d). Alternatively, samples were subjected to ICP-OES analysis to measure the concentration of Fe^{2+} (e). Data are shown as the mean ± SD of triplicate samples.

or WiDr cells in the presence or absence of various concentrations of free EGF. Cells were then subjected to immunoblotting using anti-VP1 antibody. As shown in Fig. 4d, both EGF-conjugated $VP1^{WT}$- and $VP1^{N138C}$-CMNPs much more associated with A431 cells than those of EGF-unconjugated, whereas the associations of WiDr cells with $VP1^{WT}$- and $VP1^{N138C}$-CMNPs were comparable regardless of EGF conjugation. The association of A431 cells with EGF-conjugated $VP1^{N138C}$-CMNPs was significantly inhibited by the addition of 0.3 μg free EGF and competition was saturated (Fig. 4d, lanes 15–18). A similar inhibition pattern was observed in the association between A431 cells and EGF-conjugated $VP1^{WT}$-CMNPs (Fig. 4d, lanes 6–9). On the other hand, the association of WiDr cells with either EGF-conjugated $VP1^{WT}$-CMNPs or $VP1^{N138C}$-CMNPs was hardly detected in this assay (Fig. 4d, lanes 24–27 and 33–36). These results indicate that EGF-conjugated $VP1^{N138C}$-CMNPs and $VP1^{WT}$-CMNPs specifically attach to tumor cells through the EGF-EGFR interaction. It is noteworthy that the amounts of $VP1^{N138C}$-CMNPs attached to A431 cells (lane 15) were significantly larger than those of $VP1^{WT}$-CMNPs (lanes 6), suggesting that the $VP1^{N138C}$-CMNPs target EGFR-expressing tumor cells more effectively than the $VP1^{WT}$-CMNPs.

To further evaluate the selective association, we analyzed the amount of CMNPs-derived Fe^{2+} with A431 cells using the inductively coupled plasma optical emission spectrometry (ICP-OES) analyzer (Prodigy ICP). As shown in Fig. 4e, the conjugation of EGF to $VP1^{WT}$-CMNPs and $VP1^{N138C}$-CMNPs dramatically increased the amounts of Fe^{2+} associated with A431 cells. Consistent with the data in Fig. 4d, quantification of Fe^{2+} indicated that the amount of EGF-conjugated $VP1^{N138C}$-CMNPs bound to A431 cells was 3-fold larger than that of EGF-conjugated $VP1^{WT}$-CMNPs (Fig. 4e). Moreover, the addition of 0.3 μg free EGF to this system lowered the cell-associated levels of Fe^{2+} for both $VP1^{WT}$-CMNPs and $VP1^{N138C}$-CMNPs and the competition was saturated at this concentration. Remained Fe^{2+} amounts associated with A431 cells in the range of 1 and 3 μg free EGF concentration might be due to the EGFR-nonspecific binding of $VP1^{WT}$-CMNPs and $VP1^{N138C}$-CMNPs. Taken

together, these data demonstrate that VP1^{N138C}-CMNPs are able to present EGF more effectively than VP1^{WT}-CMNPs so that the particles are targeted to EGFR-expressing tumor cells with remarkable specificity *in vitro*.

4. Conclusions

We showed that VP1 coating allows CMNPs to be monodispersed in body fluid such as serum and blood (Fig. 3a–c). This characteristic is very important for MRI contrast agents because monodispersible nanoparticles can reach tissues or organs by traveling in the blood stream. Since it has been suggested that viral capsid protein is a suitable material to achieve biocompatibility (Cormode et al., 2010), the VP1 coating may be also expected to provide biocompatibility to the nanoparticle and prevent their detection and elimination by the clearance mechanisms in the body. In addition, VP1 based architecture is shown to be very stable in broad range of salt concentration, pH, and temperature (Kawano et al., 2009) and considered to be safe for humans to use them as a vaccine material because there is no evidence that SV40 VP1 protein has acute or chronic cytotoxicity against human cells (Hilleman, 1998; Butel and Lednicky, 1999). Moreover, the VP1 coating allows further modification on the surface of CMNPs. As previously described (Bulte et al., 1994; Uchida et al., 2006), our results support that protein cages such as viral capsids or ferritins are promising platform for diagnosis use.

The most desirable feature of agents for diagnosis is the ability to target intended tissues or tumors *in vivo*. The distribution of nanoparticles in the body is affected by multiple factors such as molecular size, shape and charge (Longmire et al., 2008). For instance, certain sizes of nanoparticles tend to be accumulated in tumor tissues through enhanced permeability and retention (Maeda et al., 2000), which is known as the enhanced permeability and retention (EPR) effect (Maeda, 2001). Apart from such passive targeting, active delivery and retention of nanoparticles into tissues or tumors is still far from reality although much effort has been devoted to designing probes that detect tumors. However, active targeting is of great interest to many clinicians because this technique will allow accurate diagnosis of tumor at an early stage. Tumor-specific monoclonal antibodies may be the ultimate tool for the active targeting. A number of investigators have studied this issue using small animals (Anderson et al., 2000; Gohr-Rosenthal et al., 1993; Remsen et al., 1996; Shahbazi-Gahrouei et al., 2001; Sipkins et al., 1998; Suwa et al., 1998). However, considering the large amount of antibody used, this approach may be too costly for commercial use (Weinmann et al., 2003). On the other hand, it has been suggested that EGFR represents an ideal target for diagnosis and therapy of human carcinomas (Normanno et al., 2003; Salomon et al., 1995; Suwa et al., 1998). A majority of human solid tumors overexpress high levels of EGFR, and the overexpression level is often correlated with a poor prognosis (Salomon et al., 1995).

Because tumor cells are more heat-sensitive than normal cells, hyperthermia has served as an anti-tumor therapy (Falk and Issels, 2001; Koga et al., 1983; van der Zee, 2002). Since MNPs can be used for hyperthermia as a heater element (Gupta and Gupta, 2005), EGF-conjugated VP1^{N138C}-CMNPs may be directly applicable to tumor-targeted hyperthermia therapy. That is, EGF-immobilized VP1^{N138C}-CMNPs has a great potential for an excellent therapeutic material as well as a diagnostic material.

Acknowledgments

This work was supported by Special Coordination Funds for Promoting Science and Technology from JST, by the Global COE (Center of Excellence) Program from the Japan Ministry of Education, Culture, Sports, Science, and Technology (MEXT), and by a grant for Research and Development Projects in Cooperation with Academic Institutions from the New Energy and Technology Development Organization (to H.H.). This work was also supported by Grant-in-Aid for Scientific Research (A) (21241019 to H.H.) from MEXT.

The authors are grateful to Dr. M. Ueda (Keio University) and K. Doi, H. Kishi, K. Imai, and S. Nomura (Tokyo Institute of Technology) for providing A431 and WiDr cell lines and for the assistance of material preparation, respectively.

References

Anderson, S.A., Rader, R.K., Westlin, W.F., Null, C., Jackson, D., Lanza, G.M., Wickline, S.A., Kotyk, J.J., 2000. Magnetic resonance contrast enhancement of neovasculature with alpha(v)beta(3)-targeted nanoparticles. Magnetic Resonance in Medicine 44, 433–439.

Bulte, J.W., Douglas, T., Mann, S., Frankel, R.B., Moskowitz, B.M., Brooks, R.A., Baumgarner, C.D., Vymazal, J., Strub, M.P., Frank, J.A., 1994. Magnetoferritin: characterization of a novel superparamagnetic MR contrast agent. Journal of Magnetic Resonance Imaging 4, 497–505.

Butel, J.S., Lednicky, J.A., 1999. Cell and molecular biology of simian virus 40: implications for human infections and disease. Journal of the National Cancer Institute 91, 119–134.

Cormode, D.P., Jarzyna, P.A., Mulder, W.J., Fayad, Z.A., 2010. Modified natural nanoparticles as contrast agents for mediccal imaging. Adv. Drug Deliv. Rev. 62, 329–338.

Enomoto, T., Kukimoto, I., Kawano, M.A., Yamaguchi, Y., Berk, A.J., Handa, H., 2011. In vitro reconstitution of SV40 particles that are composed of VP1/2/3 capsid proteins and nucleosomal DNA and direct efficient gene transfer. Virology 420, 1–9.

Falk, M.H., Issels, R.D., 2001. Hyperthermia in oncology. International Journal of Hyperthermia 17, 1–18.

Garcea, R.L., Salunke, D.M., Caspar, D.L., 1987. Site-directed mutation affecting polyomavirus capsid self-assembly *in vitro*. Nature 329, 86–87.

Gohr-Rosenthal, S., Schmitt-Willich, H., Ebert, W., Conrad, J., 1993. The demonstration of human tumors on nude mice using gadolinium-labelled monoclonal antibodies for magnetic resonance imaging. Investigative Radiology 28, 789–795.

Gupta, A.K., Gupta, M., 2005. Synthesis and surface engineering of iron oxide nanoparticles for biomedical applications. Biomaterials 26, 3995–4021.

Hatakeyama, M., Kishi, H., Kita, Y., Imai, K., Nishio, K., Karasawa, S., Masaike, Y., Sakamoto, S., Sandhu, A., Tanimoto, A., Gomi, T., Kohda, E., Abe, M., Handa, H., 2011. A two-step ligand exchange reaction generates highly water-dispersed magnetic nanoparticles for biomedical applications. Journal of Materials Chemistry 21, 5959–5966.

Hilleman, M.R., 1998. Discovery of simian virus 40 (SV40) and its relationship to poliomyelitis virus vaccines. Developments in Biological Standardization 94, 183–190.

Hirabayashi, K., Yano, J., Inoue, T., Yamaguchi, T., Tanigawara, K., Smyth, G.E., Ishiyama, K., Ohgi, T., Kimura, K., Irimura, T., 1999. Inhibition of cancer cell growth by polyinosinic–polycytidylic acid/cationic liposome complex: a new biological activity. Cancer Research 59, 4325–4333.

Inoue, T., Kawano, M.A., Takahashi, R.U., Tsukamoto, H., Enomoto, T., Imai, T., Kataoka, K., Handa, H., 2008. Engineering of SV40-based nano-capsules for delivery of heterologous proteins as fusions with the minor capsid proteins VP2/3. Journal of Biotechnology 134, 181–192.

Ishizu, K.I., Watanabe, H., Han, S.I., Kanesashi, S.N., Hoque, M., Yajima, H., Kataoka, K., Handa, H., 2001. Roles of disulfide linkage and calcium ion-mediated interactions in assembly and disassembly of virus-like particles composed of simian virus 40 VP1 capsid protein. Journal of Virology 75, 61–72.

Kanesashi, S.N., Ishizu, K., Kawano, M.A., Han, S.I., Tomita, S., Watanabe, H., Kataoka, K., Handa, H., 2003. Simian virus 40 VP1 capsid protein forms polymorphic assemblies *in vitro*. Journal of General Virology 84, 1899–1905.

Kawano, M.A., Inoue, T., Tsukamoto, H., Takaya, T., Enomoto, T., Takahashi, R.U., Yokoyama, N., Yamamoto, N., Nakanishi, A., Imai, T., Wada, T., Kataoka, K., Handa, H., 2006. The VP2/VP3 minor capsid protein of simian virus 40 promotes the *in vitro* assembly of the major capsid protein VP1 into particles. Journal of Biological Chemistry 281, 10164–10173.

Kawano, M.A., Xing, L., Tsukamoto, H., Inoue, T., Handa, H., Cheng, R.H., 2009. Calcium bridge triggers capsid disassembly in the cell entry process of simian virus 40. Journal of Biological Chemistry 284, 34703–34712.

Kitai, Y., Fukuda, H., Enomoto, T., Asakawa, Y., Suzuki, T., Inouye, S., Handa, H., 2011. Cell selective targeting of a simian virus 40 virus-like particle conjugated to epidermal growth factor. Journal of Biotechnology 155, 251–256.

Koga, S., Izumi, A., Maeta, M., Shimizu, N., Osaki, Y., Kanayama, H., 1983. The effects of total-body hyperthermia combined with anticancer drugs on immunity in advanced cancer patients. Cancer 52, 1173–1177.

Kosukegawa, A., Arisaka, F., Takayama, M., Yajima, H., Kaidow, A., Handa, H., 1996. Purification and characterization of virus-like particles and pentamers produced by the expression of SV40 capsid proteins in insect cells. Biochimica et Biophysica Acta 1290, 37–45.

Liddington, R.C., Yan, Y., Moulai, J., Sahli, R., Benjamin, T.L., Harrison, S.C., 1991. Structure of simian virus 40 at 3.8-A resolution. Nature 354, 278–284.

Longmire, M., Choyke, P.L., Kobayashi, H., 2008. Clearance properties of nano-sized particles and molecules as imaging agents: considerations and caveats. Nanomedicine (Lond) 3, 703–717.

Maeda, H., 2001. The enhanced permeability and retention (EPR) effect in tumor vasculature: the key role of tumor-selective macromolecular drug targeting. Advances in Enzyme Regulation 41, 189–207.

Maeda, H., Wu, J., Sawa, T., Matsumura, Y., Hori, K., 2000. Tumor vascular permeability and the EPR effect in macromolecular therapeutics: a review. Journal of Controlled Release 65, 271–284.

Montet, X., Montet-Abou, K., Reynolds, F., Weissleder, R., Josephson, L., 2006. Nanoparticle imaging of integrins on tumor cells. Neoplasia 8, 214–222.

Nasongkla, N., Bey, E., Ren, J., Ai, H., Khemtong, C., Guthi, J.S., Chin, S.F., Sherry, A.D., Boothman, D.A., Gao, J., 2006. Multifunctional polymeric micelles as cancer-targeted, MRI-ultrasensitive drug delivery systems. Nano Letters 6, 2427–2430.

Noguchi, P., Wallace, R., Johnson, J., Earley, E.M., O'Brien, S., Ferrone, S., Pellegrino, M.A., Milstien, J., Needy, C., Browne, W., Petricciani, J., 1979. Characterization of the WIDR: a human colon carcinoma cell line. In Vitro 15, 401–408.

Normanno, N., Maiello, M.R., De Luca, A., 2003. Epidermal growth factor receptor tyrosine kinase inhibitors (EGFR-TKIs): simple drugs with a complex mechanism of action? Journal of Cellular Physiology 194, 13–19.

Remsen, L.G., McCormick, C.I., Roman-Goldstein, S., Nilaver, G., Weissleder, R., Bogdanov, A., Hellstrom, I., Kroll, R.A., Neuwelt, E.A., 1996. MR of carcinoma-specific monoclonal antibody conjugated to monocrystalline iron oxide nanoparticles: the potential for noninvasive diagnosis. American Journal of Neuroradiology 17, 411–418.

Salomon, D.S., Brandt, R., Ciardiello, F., Normanno, N., 1995. Epidermal growth factor-related peptides and their receptors in human malignancies. Critical Reviews in Oncology/Hematology 19, 183–232.

Shahbazi-Gahrouei, D., Williams, M., Rizvi, S., Allen, B.J., 2001. In vivo studies of Gd-DTPA-monoclonal antibody and gd-porphyrins: potential magnetic resonance imaging contrast agents for melanoma. Journal of Magnetic Resonance Imaging 14, 169–174.

Sipkins, D.A., Cheresh, D.A., Kazemi, M.R., Nevin, L.M., Bednarski, M.D., Li, K.C., 1998. Detection of tumor angiogenesis *in vivo* by alphaVbeta3-targeted magnetic resonance imaging. Nature Medicine 4, 623–626.

Suwa, T., Ozawa, S., Ueda, M., Ando, N., Kitajima, M., 1998. Magnetic resonance imaging of esophageal squamous cell carcinoma using magnetite particles coated with anti-epidermal growth factor receptor antibody. International Journal of Cancer 75, 626–634.

Takahashi, R.U., Kanesashi, S.N., Inoue, T., Enomoto, T., Kawano, M.A., Tsukamoto, H., Takeshita, F., Imai, T., Ochiya, T., Kataoka, K., Yamaguchi, Y., Handa, H., 2008. Presentation of functional foreign peptides on the surface of SV40 virus-like particles. Journal of Biotechnology 135, 385–392.

Tsukamoto, H., Kawano, M.A., Inoue, T., Enomoto, T., Takahashi, R.U., Yokoyama, N., Yamamoto, N., Imai, T., Kataoka, K., Yamaguchi, Y., Handa, H., 2007. Evidence that SV40 VP1-DNA interactions contribute to the assembly of 40-nm spherical viral particles. Genes to Cells 12, 1267–1279.

Uchida, M., Flenniken, M.L., Allen, M., Willits, D.A., Crowley, B.E., Brumfield, S., Willis, A.F., Jackiw, L., Jutila, M., Young, M.J., Douglas, T., 2006. Targeting of cancer cells with ferrimagnetic ferritin cage nanoparticles. Journal of the American Chemical Society 128, 16626–16633.

van der Zee, J., 2002. Heating the patient: a promising approach? Annals of Oncology 13, 1173–1184.

Weinmann, H.J., Ebert, W., Misselwitz, B., Schmitt-Willich, H., 2003. Tissue-specific MR contrast agents. European Journal of Radiology 46, 33–44.

Yokoyama, N., Kawano, M.A., Tsukamoto, H., Enomoto, T., Inoue, T., Takahashi, R.U., Nakanishi, A., Imai, T., Wada, T., Handa, H., 2007. Mutational analysis of the carboxyl-terminal region of the SV40 major capsid protein VP1. Journal of Biochemistry 141, 279–286.

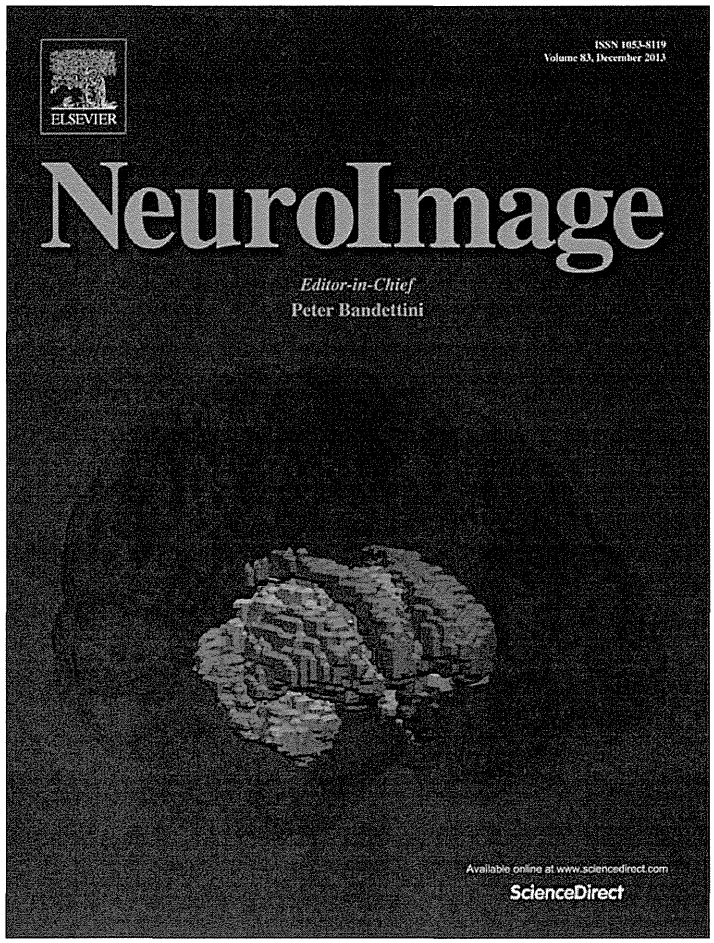

NeuroImage 83 (2013) 294–306

Contents lists available at ScienceDirect

NeuroImage

journal homepage: www.elsevier.com/locate/ynimg

MRI-based morphometric characterizations of sexual dimorphism of the cerebrum of ferrets (*Mustela putorius*)

Kazuhiko Sawada [a,*], Miwa Horiuchi-Hirose [b], Shigeyoshi Saito [c], Ichio Aoki [d]

[a] Department of Physical Therapy, Faculty of Medical and Health Sciences, Tsukuba International University, Tsuchiura, Ibaraki 300-0051, Japan
[b] Department of Nutrition, Faculty of Medical and Health Sciences, Tsukuba International University, Tsuchiura, Ibaraki 300-0051, Japan
[c] Department of Medical Engineering, Division of Health Sciences, Osaka University Graduate School of Medicine, Suita, Osaka 565-0871, Japan
[d] Molecular Imaging Center, National Institute of Radiological Sciences, Chiba 263-8555, Japan

ARTICLE INFO

Article history:
Accepted 3 June 2013
Available online 14 June 2013

Keywords:
Phylogeny
Evolution
Brain
Neurodevelopmental disorders
Sexual dimorphism

ABSTRACT

The present study aimed to characterize cerebral morphology in young adult ferrets and its sexual dimorphism using high-field MRI and MRI-based morphometry. *Ex vivo* short TR/TE (typical T_1-weighted parameter setting for conventional MRI) and T_2W (long TR/TE) MRI with high spatial resolution at 7-tesla could visualize major subcortical and archicortical structures, i.e., the caudate nucleus, lentiform nucleus, amygdala and hippocampus. In particular, laminar organization of the olfactory bulb was identifiable by short TR/TE-MRI. The primary and secondary sulci observable in the adult ferret were distinguishable on either short TR/TE- or T_2W-MRI, and the cortical surface morphology was reproduced well by 3D-rendered images obtained by short TR/TE-MRI. The cerebrum had a significantly lower volume in females than in males, which was attributed to region-specific volume reduction in the cerebral cortex and subcortical white matter in females. A sexual difference was also detected, manifested by an overall reduction in normalized signal ratios of short TR/TE-MRI in all cerebral structures examined in females than in males. On the other hand, an alternating array of higher and lower short TR/TE-MRI intensity transverse zones throughout the cortex, which was reminiscent of the functional cortical areas, was revealed by maximum intensity projection (MIP) in 3D. The normalized signal ratio of short TR/TE-MRI, but not T_2W-MRI in the cortex, was negatively correlated with the density of myelin-basic protein immunoreactive fibers (males, $r = -0.440$; females, $r = -0.481$). The present results suggest that sexual differences in the adult ferret cerebrum are characterized by reduced volumes of the cerebral cortex and subcortical white matter in females, and by overall reductions in physiochemical characteristics, as obtained by short TR/TE-MRI, in females. It should be noted that short TR/TE-MRI-based MIP delineated functional cortical areas related to myeloarchitecture in 3D. Such an approach makes possible conventional investigation of the functional organization of the cerebral cortex and its abnormalities using high-field MRI.

Introduction

The remarkable development and spread of imaging techniques such as MRI and CT in recent years have provided full 3D brain coverage, while leaving the gross anatomy conserved. Quantitative analysis methods using these imaging techniques allow the investigation of focal differences in brain structures between a control and experimental group, or time-dependent changes in brain structures within groups (Wright et al., 1995). A number of studies have been attempted to explain structural sexual dimorphism of brain regions, quantitatively. Sex differences are noted in volumes of particular regions of the cerebral cortex, hippocampus, caudate nucleus, globus pallidus and/or olfactory bulb in humans (Carne et al., 2006; Giedd et al., 1997; Suzuki et al., 2005) and mice (Schlaepfer et al., 1995; Spring et al., 2007). Several studies revealed that sex-related volume changes in specific regions of the brain are involved in neurodevelopmental and psychological disorders such as schizophrenia (Exner et al., 2008), amnestic mild cognitive impairment, Alzheimer's disease

Abbreviations: A1, primary auditory cortex; aad, anterior ancinate dimple; AAF, anterior auditory field; ac, anterior commissure; aci, intrabulbar anterior commissure; ADF, anterior dorsal field; as, ancinate sulcus; AEG, anterior ectosylvian gyrus; ASG, anterior sigmoid gyrus; Amg, amygdala; AVF, anterior ventral field; cc, corpus callosum; Cd, caudate nucleus; cg, cingulum; CNG, coronal gyrus; cns, coronal sulcus; crs, cruciate sulcus; csss, caudal suprasylvian sulcus; ec, external capsule; EPl, external plexiform layer; Gl, glomerular layer; Hip, hippocampus; ic, internal capsule; IPl, internal plexiform layers; LG, lateral gyrus; Ln, lentiform nucleus; ls, lateral sulcus; M1, primary motor cortex; MBP, myelin basic protein; Mi, mitral layer; MIP, maximum intensity projection; Ob, olfactory bulb; Obc, olfactory bulb core; OBG, orbital gyrus; OD, optical density; opr, optic radiation; ots, occipitotemporal sulcus; oSVZ, outer subventricular zone; PEG, posterior ectosylvian gyrus; PFA, paraformaldehyde; PPr, rostral posterior parietal cortex; prs, presylvian sulcus; PPF, posterior pseudosylvian field; prs, presylvian sulcus; PSF, posterior suprasylvian field; PSG, posterior sigmoid gyrus; pss, pseudosylvian sulcus; rf, rhinal fissure; rs, rhinal sulcus; rsss, rostral suprasylvian sulcus; spt, septum; S1, primary somatosensory cortex; SII, secondary somatosensory cortex; SIII, third somatosensory cortex; SSG, suprasylvian gyrus; subWM, subcortical matter; ss, splenial sulcus; Th, thalamus; VCA, visual cortical area.

* Corresponding author at: Department of Physical Therapy, Faculty of Medical and Health Sciences, Tsukuba International University, 6-8-33 Manabe, Tsuchiura, Ibaraki 300-0051, Japan. Fax: +81 29 826 6776.
E-mail address: k-sawada@tius-hs.jp (K. Sawada).

1053-8119/$ – see front matter © 2013 Elsevier Inc. All rights reserved.
http://dx.doi.org/10.1016/j.neuroimage.2013.06.024

(Skup et al., 2011), and panic disorder (Asami et al., 2009) in humans. In addition, a higher prevalence of autism is found in males than in females, and appears to show abnormalities in the cerebral cortical surface morphology (Harden et al., 2004; Levitt et al., 2003). Therefore, quantitative data regarding sexual dimorphism of various regions provide fundamental information for investigating the pathogenesis of sex-related neurodevelopmental and psychological disorders.

Ferrets (*Mustela putorius*) are the smallest laboratory animals that have a highly convoluted surface of the cerebrum, forming striking patterns of sulci and gyri (Lawes and Andrews, 1998). This animal has advantages as an experimental model for studying the plasticity and development of the central nervous system. Neurodevelopmental events occurring *in utero* in primates, such as the early stage of neurogenesis (Clancy et al., 2001), sulcal infolding (Sawada and Watanabe, 2012; Smart and McSherry, 1986), and the transient appearance of the outer subventricular zone (oSVZ) with basal radial glia (Fietz et al., 2010; Martínez-Cerdeño et al., 2012), are experienced in ferrets following birth. This means that experimental magnifications such as drug administration and stress loading can be applied directly to the pups. Furthermore, ferrets are used as an animal model for a debilitating respiratory disease, human influenza, because of their high sensitivity to infection by human influenza viruses and diseases closely resembling human influenza (Maher and DeStefano, 2004). This means that ferrets have the potential for application to studies of influenza-associated encephalopathy. The present study aimed to characterize the cerebral morphology in young adult ferrets and its sexual dimorphism using MRI-based morphometry. To achieve a sufficient resolution for determining individual structures, fixed forebrain was examined using a high spatial resolution 7-tesla MRI system.

Materials and methods

Samples

The present study used cerebra from male and female ferrets at postnatal day (PD) 90 (male, n = 5; female, n = 5) that had been previously used in our gross anatomical examination of cerebral surface morphology (Sawada and Watanabe, 2012). Briefly, the animals were deeply anesthetized with an intraperitoneal injection of chloral hydrate (400 μg/g body weight), and were perfused with 0.9% NaCl followed by 4% paraformaldehyde (PFA) in a 10 mM phosphate buffer, pH 7.4. Brains were removed from skulls, and immersed in the same fixative.

MRI measurements

Three-dimensional T_1-weighted (short TR/TE) and two-dimensional T_2W (long TR/TE) MRI were performed with a 7.0-T MRI system (Magnet; Kobelco and Jastec, Kobe, Japan) (Console; Bruker BioSpin, Ettlingen, Germany). A birdcage RF coil for transmission and reception (70-mm inner diameter, Rapid Biomedica; or 60-mm inner diameter, Bruker BioSpin) was used with a field of view adequate for the sample dimensions. Slice orientation (transaxial) was precisely adjusted for the cerebral base using pilot-MR images obtained by gradient-echo sequence. A three-dimensional T_1-weighted image covering the entire brain was acquired using the rapid acquisition with relaxation enhancement (RARE) sequence, with the following parameters: repetition time (TR) = 300 ms, echo time (TE) = 9.6 ms (effective TE = 19.2 ms), RARE factor = 4, field of view (FOV) = 32 × 32 × 40 mm^3, acquisition matrix = 256 × 256 × 256, voxel size = 125 × 125 × 156 μm^3, number of acquisitions (NEX) = 2, and total scan time = 2 h 43 min 50 s. A multi-slice T_2-weighted image covering the entire brain was acquired using the RARE sequence with the following parameters: repetition time TR = 4200 ms, TE = 12 ms (effective TE = 36 ms), rare factor = 8, FOV = 38.4 × 38.4 mm^2, slice thickness = 1.0 mm, slice gap = 1.5 mm, number of slices = 10, acquisition matrix = 256 × 192 (reconstructed to 256 × 256 using zero-filling method), voxel size = 150 × 150 × 1000 μm^3, NEX = 40, and total scan time = 1 h 7 min 12 s.

We used the term "short TR/TE MRI" in the context of "MRI measured using typical T_1W parameter setting" in the present study, because the T_1W parameter setting did not show T_1-weighted contrast at the PFA-fixed brain sample under high-field MRI. Although shorter T_1 tissue, such as white matter, must be enhanced on T_1W-MRI, the signal was reduced due to the short T_2 of PFA solution (Supplement 1).

3D volume-rendered images

All 3D data were used for volumetric analysis. The cerebral cortex, olfactory bulb, caudate nucleus, lentiform nucleus (putamen plus globus pallidus), amygdala and hippocampus were semi-automatically segmented on MRI images using the "Morpho" tool of SliceOmatic software ver 4.3 (TomoVision, Montreal, Canada) based on image contrast as well as the user's knowledge of the anatomy. Segmented images were then analyzed using the 3D-rendering module of the same software. The cerebral image was rendered in 3D using the surface projection algorithm which best visualized the surface and sulci of the cerebrum. The 3D-rendered images were then rotated and manipulated in a manner that best visualized brain morphology by a linear registration method using SliceOmatic software. A clear indentation at the cerebral surface was considered the indication of a sulcus. A gyrus was defined as any tissue delimited by two or more fissures, sulci, or dimples. The terminology and identification of cerebral sulci and gyri were based on the textbook of Lawes and Andrews (1998).

Volumetric analysis

Areas of the segmented regions of each cerebral region were measured using SliceOmatic software. The volumes were calculated by multiplying the combined areas by the slice thickness (156.25 μm) with the total areas of those regions being regarded as the volume of the whole cerebrum. Data on the volume of each cerebral structure of the left and right hemispheres were analyzed separately.

Data analysis of short TR/TE and T_2W-MRI

Signal levels of short TR/TE and T_2W-MRI intensity were quantified by specifying the region of interest (ROI) in the known cortical areas, and in the major subcortical and archicortical structures. The following cortical regions were selected on the maximum intensity projection (MIP) color map by registration using the "Point" tool of SliceOmatic software for specifying the ROI, and signal intensities in each ROI: the primary motor cortex (M1; the rostral halves of posterior sigmoid gyrus (PSG) and coronal gyrus (CNG)), secondary somatosensory cortex (SII; the rostral half of the anterior ectosylvian gyrus (AEG)), primary auditory cortex (A1; the upper half of posterior ectosylvian gyrus (PEG)) as the cortical areas exhibiting a relatively low short TR/TE intensity, primary somatosensory cortex (S1; the caudal halves of PSG and CNG), rostral posterior parietal cortex (PPr; the rostral half of lateral gyrus (LG)), and area 17 (the caudal half of the visual cortical area (VCA)) as the cortical areas exhibiting a relatively high short TR/TE-MRI intensity. Intensities of short TR/TE- and T_2W-MRI were measured as background signals in the medium (4% PFA solution) that filled the brains. We defined the ROIs for the background signal at the points nearest (within 2–10 mm apart on the same coronal images) of ROIs for each brain region, in order to minimize the effect of RF inhomogeneity. Typical localizations of ROIs in each brain region and the respective background signals are shown in Supplement 2. The normalized signal ratios of short TR/TE and T_2W-MRI intensity were calculated by a formula [(signal intensity in the brain region) / (signal intensity of the nearest medium)]. Here, we carefully assessed the RF coil inhomogeneity (B_1 profile;

see Supplement 3). In our measurement conditions, inhomogeneity in the RF coil's B_1 field was very low in both T_1W (short TR/TE) MRI intensity (S.D. ratio = 0.0226) and T_2W-MRI intensity (S.D. ratio = 0.0479), suggesting that there was no serious signal inhomogeneity at the ROIs both in the brain and background medium. S.D. ratio indicates [(standard deviation of all ROIs)/(mean of all ROIs)].

Furthermore, the normalized signal ratios of short TR/TE and T_2W-MRI intensity were represented on coronal and axial images using a color-scale ("gray level intensity color map" module, SliceOmatic software).

A MIP color map was made from the segmented images of the cerebral cortex on short TR/TE MRI using the MIP module of the

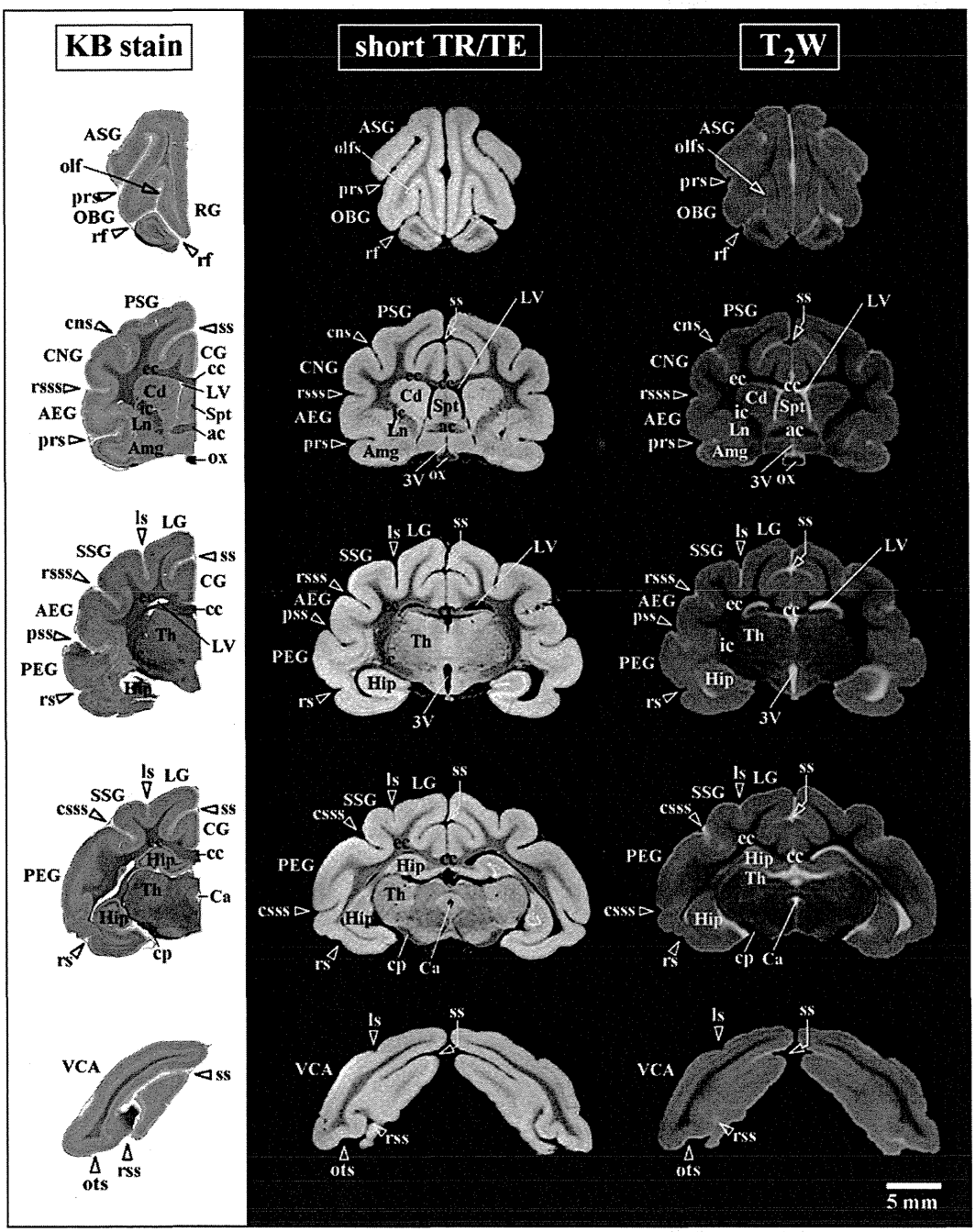

Fig. 1. Representative coronal short TR/TE-MRI (typical T_1-weighted parameter setting for conventional MRI) and T_2W-MRI (long TR/TE) images of adult male ferret cerebrum with identical planes of Klüver–Barrera stained sections. (A) Klüver–Barrera stained sections, (B) short TR/TE-MRI images, and (C) T_2W-MRI images. Both short TR/TE- and T_2W-MRI visualized major subcortical and archicortical structures, and all primary sulci and dimples. The T_1W parameter setting (short TR/TE) did not show T_1-weighted contrast at the PFA-fixed brain sample under high-field MRI in the present study. Although shorter T_1 tissue, such as white matter, must be enhanced on T_1W-MRI, the signal was reduced due to the short T_2 of PFA solution (Supplement 1). 3V, third ventricle; ac, anterior commissure; AEG, anterior ectosylvian gyrus; Amg, amygdala; as, ancinate sulcus; ASG, anterior sigmoid gyrus; Ca, cerebral aqueduct; cc, corpus callosum; Cd, caudate nucleus; CG, cingulate gyrus; CNG, coronal gyrus; cns, coronal sulcus; cp, cerebral peduncle; csss, caudal suprasylvian sulcus; ec, external capsule; Hip, hippocampus; ic, internal capsule; LG, lateral gyrus; Ln, lentiform nucleus; LV, lateral ventricle; OBG, orbital gyrus; olf, olfactory sulcus; ots, occipitotemporal sulcus; ox, optic chiasma; PEG, posterior ectosylvian gyrus; PFA, paraformaldehyde; prs, presylvian sulcus; PSG, posterior sigmoid gyrus; rf, rhinal fissure; RG, rectal gyrus; rsss, rostral suprasylvian sulcus; rs, rhinal sulcus; spt, septum; ss, splenial sulcus; SSG, suprasylvian gyrus; Th, thalamus; VCA, visual cortical area.

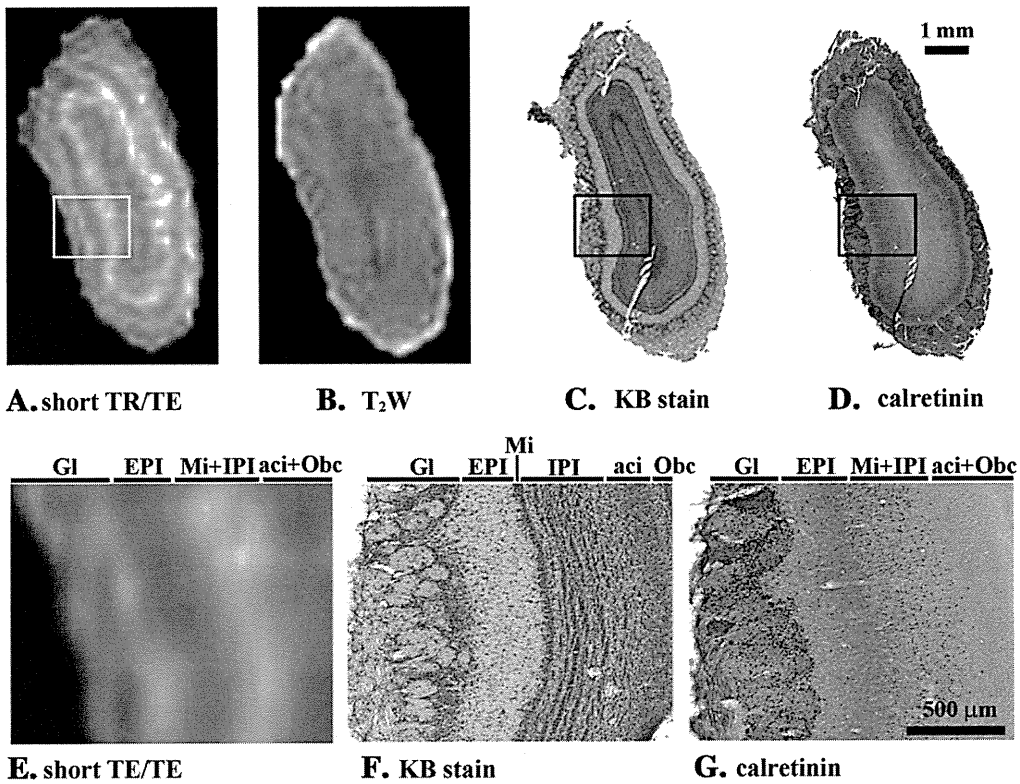

Fig. 2. Representative short TR/TE-MRI (typical T_1-weighted parameter setting for conventional MRI) and T_2W-MRI (long TR/TE) images of olfactory bulb of adult male ferrets with identical planes of Klüver–Barrera stained and calretinin-immunostained sections. (A) Short TR/TE-MRI image, (B) T_2W-MRI image, (C) Klüver–Barrera stained section, and (D) calretinin-immunostained section. (E) Boxed areas of short TR/TE-MRI image of (A) at high magnification. (F) Boxed areas of Klüver–Barrera stained and section of (C) at high magnification. (G) Boxed areas of calretinin-immunostained section of (D) at high magnification. The T_1W parameter setting (short TR/TE) did not show T_1-weighted contrast at the PFA-fixed brain sample under high-field MRI in the present study. Although shorter T_1 tissue, such as white matter, must be enhanced on T_1W-MRI, the signal was reduced due to the short T_2 of PFA solution (Supplement 1). Some layers of olfactory bulb were distinguishable by short TR/TE-MRI. aci, intrabolbar acinar commissure; EPI, external plexiform layer; Gl, glomerular layer; IPI, internal plexiform layer; Mi, mitral layer; Obc, olfactory bulb core, PFA, paraformaldehyde.

SliceOmatic software. MIP is a volume visualization method for 3D data that projects in the visualization plane the voxels with the maximum intensity that fall in the way of parallel rays traced from the viewpoint to the plane of projection.

Histology and immunohistochemistry

Following MRI measurements, right and left cerebral hemispheres were separated at the longitudinal cerebral fissure, and were cryoprotected by

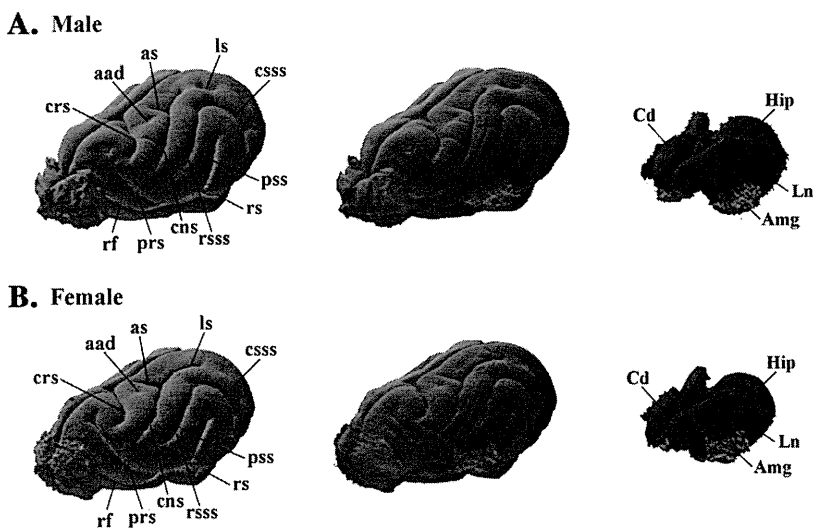

Fig. 3. Volume-rendered images in cerebra of male and female ferrets. (A) Three-dimensional volume-rendered images of male cerebrum. (B) Three-dimensional volume-rendered images of female cerebrum. Left images of (A) and (B) are reconstructed images of cerebral cortex and olfactory bulb (Ob); middle images of (A) and (B) are reconstructed images of all cerebral structures rendered. Right images of (A) and (B) are reconstructed images of caudate nucleus (Cd; red), lentiform nucleus (Ln; blue), amygdala (Amg; green) and hippocampus (Hip; purple). aad, anterior ancinate dimple; as, ancinate sulcus; cns, coronal sulcus; crs, cruciate sulcus; csss, caudal suprasylvian sulcus; prs, presylvian sulcus; pss, pseudosylvian sulcus; rf, rhinal fissure; rs, rhinal sulcus; rsss, rostral suprasylvian sulcus; subWM, subcortical matter.

immersion in 30% sucrose in 10 mM phosphate-buffered saline (PBS) overnight. The cerebral hemispheres were frozen in optimal cutting temperature embedding compound, and sectioned serially in the coronal plane at 40 μm by a Retratome (REM-700; Yamato Koki Industrial, Asaka, Japan) with a refrigeration unit (Electro Freeze MC-802A, Yamato Koki Industrial Co., Ltd.). Some sections were stained with Klüver–Barrera according to protocols of Sheehan and Hrapchak (1980) as an anatomical reference to MRI images.

All immunohistochemical procedures were performed on floating sections. The sections were immersed in 3% H_2O_2 in PBS containing 0.1% Triton X-100 for the inactivation of endogenous peroxidase. After washing with PBS, sections were reacted with a rabbit anti-calretinin polyclonal antibody (1:10,000; Swant, Switzerland), or a rat anti-myelin basic protein (MBP) monoclonal antibody (Millipore, Billerica, CA, USA), containing 10% normal goat serum at 4 °C overnight. Those two antibodies produced highly specific immunostaining in the ferret tissues in previous studies (Poluch et al., 2008; Tao et al., 2012). After incubation, the sections were rinsed with PBS and reacted with biotinylated anti-rabbit IgG or biotinylated anti-rat IgG. The immunoreactive products were visualized by a Vectastain ABC elite kit (Vector Labs., Inc., Burlingame, CA) using 0.01% 3,3′-diaminobenzidine tetrachloride (Sigma) in 0.03% H_2O_2 as a chromogen.

To enable a comparison of MBP immunoreactive fiber density, all sections were processed in identical staining conditions. Evaluation of MBP immunoreactive fibers in the cerebral cortex was performed by using a modified protocol designed for our previous study (Koyanagi et al., 2006). Captured images of the MBP immunostained sections of the identical regions of the cortex, which were used to calculate the normalized ratios of short TR/TE- and T_2W-MRI intensity in the primary motor cortex (M1; the rostral halves of PSG and CNG), primary somatosensory cortex (S1; the caudal halves of PSG and CNG), secondary somatosensory cortex (SII; the rostral half of the AEG), primary auditory cortex (A1; the upper half of PEG), rostral posterior parietal cortex (PPr; the rostral half of LG), and area 17 (the caudal half of the VCA), were converted to black and white images. The optical density (OD) within a rectangular frame at a width of 200 μm and a length covering the entire depth of the cortex was measured in each cortical area as the MBP immunoreactive fiber density using ImageJ software (National Institutes of Health, Bethesda, USA). The mean of five points more than 30 μm apart was used for each animal when measuring the OD.

Table 1
Absolute volumes, % of total cerebral volume, and % larger in male volumes of cerebral structures in ferrets.

	n=	Absolute volume (mm^3)	% of total cerebral volume	% larger in male volumes
Cerebrum				
Male	10	2,139 ± 113.1#	–	10.8
Female	10	1,930 ± 117.4	–	–
Cortex				
Male	10	1,317 ± 92.0***	61.5 ± 1.45***	8.4
Female	10	1,214 ± 80.5	62.9 ± 0.69	–
Olfactory bulb				
Male	10	104 ± 9.0	4.9 ± 0.52	6.4
Female	10	98 ± 6.2	5.1 ± 0.36	–
Caudate nucleus				
Male	10	62 ± 3.4	2.9 ± 0.22	7.9
Female	10	58 ± 3.3	3.0 ± 0.16	–
Lentiform nucleus				
Male	10	62 ± 5.7	2.9 ± 0.30	17.0
Female	10	53 ± 4.3	2.7 ± 0.14	–
Amygdala				
Male	10	43 ± 2.7	2.0 ± 0.15	−0.9
Female	10	43 ± 3.6	2.2 ± 0.23	–
Hippocampus				
Male	10	93 ± 5.3	4.3 ± 0.32	11.7
Female	10	83 ± 7.7	4.3 ± 0.42	–
Subcortical white matter				
Male	10	312 ± 32.9**	14.6 ± 1.22*	15.4
Female	10	271 ± 23.8	14.0 ± 0.85	–

All measurements of the left and right hemispheres were quantified separately in males (n = 5) and females (n = 5), and data on each side were considered to be "n = 1."
Results of volumes of each cerebral structure and % of cerebral volume are presented as mean ± S.D. Results of % larger volumes in males than in females are presented.
# $P < 0.001$ vs. females (Student's *t*-test).
* $P < 0.05$ vs. females (*Fisher's* LSD test).
** $P < 0.01$ vs. females (*Fisher's* LSD test).
*** $P < 0.001$ vs. females (*Fisher's* LSD test).

Statistical analysis

All measurements of the left and right hemispheres were quantified separately. This was followed by a paired sampled *t*-test that demonstrated no significant left/right differences, and data on each side were considered to be "n = 1." Sex-related changes in each parameter were statistically evaluated by two-way ANOVA using both sexes and brain regions (gray and white matter structures or cortical areas) as factors. Then, as post-hoc testing, *Fisher's* LSD test was used to compare males and females.

Ethics

The experimental procedures in the present study were conducted in accordance with the guidelines of the National Institutes of Health (NIH) for the Care and Use of Laboratory Animals. The Institutional

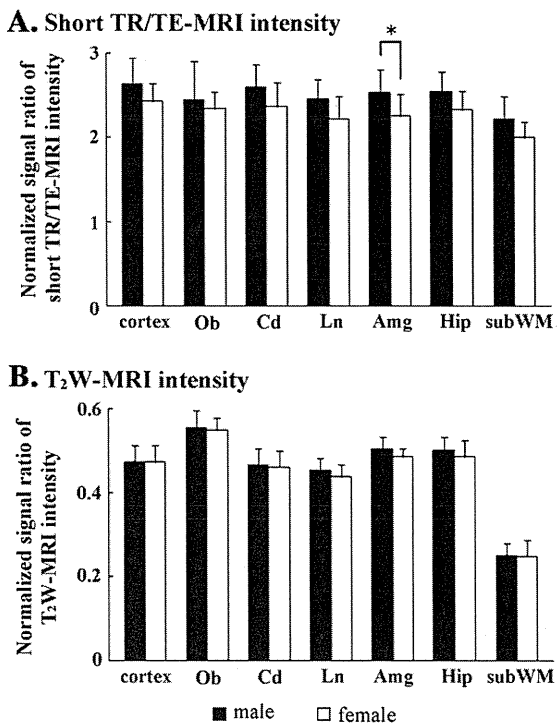

Fig. 4. Bar graphs for normalized signal ratios of short TR/TE (typical T_1-weighted parameter setting for conventional MRI) and T_2W (long TR/TE) MRI intensity in cerebral cortex, and subcortical and archicortical structures of male and female ferrets. Measurements of left and right hemispheres were quantified separately in males (n = 5) and females (n = 5), and data on each side of the hemispheres were considered to be "n = 1." (A) Normalized signal ratios of short TR/TE-MRI intensity. For short TR/TE-MRI, two-way ANOVA revealed significant effects on sexes ($F_{1,126} = 18.401$, $P < 0.001$) and cerebral structures ($F_{6,126} = 4.338$, $P < 0.001$), but not on their interaction. (B) Normalized signal ratios of T_2W-MRI intensity. For T_2W-MRI, two-way ANOVA revealed significant effects on cerebral structures ($F_{6,126} = 124.329$, $P < 0.001$), but not on sexes and their interaction. *: $P < 0.05$ (*Fisher's* LSD test). Amg, amygdala; Cd, caudate nucleus; Hip, hippocampus; Ln, lentiform nucleus; Ob, olfactory bulb; subWM, subcortical white matter.

Animal Care and Use Committee of Tsukuba International University approved the procedures, and all efforts were made to minimize the number of animals used and their suffering.

Results

Images of short TR/TE and T_2W-MRI

Representative images from coronal short TR/TE- and T_2W-MRI of adult male ferrets' cerebra were shown in Fig. 1. The T_1W parameter setting (short TR/TE) did not show T_1-weighted contrast at the PFA-fixed brain sample under high-field MRI in the present study. Although shorter T_1 tissue, such as white matter, must be enhanced on T_1W-MRI, the signal was reduced due to the short T_2 of PFA solution (Fig. 1, Supplement 1). Klüver–Barrera staining was conducted for anatomical reference. Both short TR/TE- and T_2W-MRI visualized major subcortical and archicortical structures, i.e., the caudate nucleus (Cd), the lentiform nucleus (Ln), the amygdala (Amg) and the hippocampus (Hip). Subcortical matter (SubWM), including a corpus callosum (cc) and external capsule (ec), was also delineated. The cerebral cortex was clearly distinguishable by having a relatively high signal intensity of short TR/TE- and T_2W-MRI compared to the adjacent white matter. All primary sulcus and dimples observed on gross observations previously (Sawada and Watanabe, 2012) were identifiable on either short TR/TE- or T_2W-MRI.

In the olfactory bulb (Ob), four layers with the higher and lower short TR/TE-MRI signals aligned alternately from the outer surface (Fig. 2). An observation of such an array of layers was unclear by T_2W-MRI (Fig. 2). In order to identify short TR/TE-MRI-defined layers of the olfactory bulb, MRI images were compared with the identical plane of Klüver–Barrera-stained sections. The outermost layers with high signal intensity and the second layer with low signal intensity corresponded to the glomerular layer (Gl) and the external plexiform layer (EPI), respectively. The third layer with high signal intensity was seen through the mitral (Mi) and internal plexiform layers (IPI). A boundary to those two layers was not delineated by short TR/TE-MRI. Likewise, the fourth layer with low signal intensity was seen through the white matter bundles of intrabulbar anterior commissure (aci) and the olfactory bulb core (Obc), with no demarcation of their boundary by short TR/TE-MRI. Furthermore, we carried out immunostaining for calretinin, which is a specific marker for interneurons of the Gl and IPI. Consistent with findings by Klüver–Barrera staining, the superficial and third layers representing higher short TR/TE-MRI signals corresponded to the Gl and IPI, which contained a high density of calretinin-immunoreactive small neurons (Fig. 2).

3D reconstruction and volumetric analysis

Three-dimensional volume-rendered images of the cerebrum of male and female ferrets were calculated using short TR/TE-MRI. The rendered images reproduced the cerebral cortical morphology well, with the primary and secondary sulci observable in the adult ferrets (Fig. 3). The cerebral volume was significantly lower in females than in males ($P < 0.001$) (Table 1). The 3D morphology and topology of major subcortical and archicortical structures, i.e., the olfactory bulb, caudate nucleus, lentiform nucleus, amygdala and hippocampus, were also obtained by the rendered images (Fig. 3). We calculated the volumes of those structures in male and female ferrets. Two-way ANOVA revealed significant effects on sexes ($F_{1,126} = 17.707$, $P < 0.001$) and cerebral structures ($F_{6,26} = 3298.686$, $P < 0.001$), and the interactions of those two factors ($F_{6,26} = 5.624$, $P < 0.001$). Region-specific sexual difference was detected by significantly lower volumes of cerebral cortex ($P < 0.001$) and subcortical white matter ($P < 0.01$) in females than males by post-hoc testing.

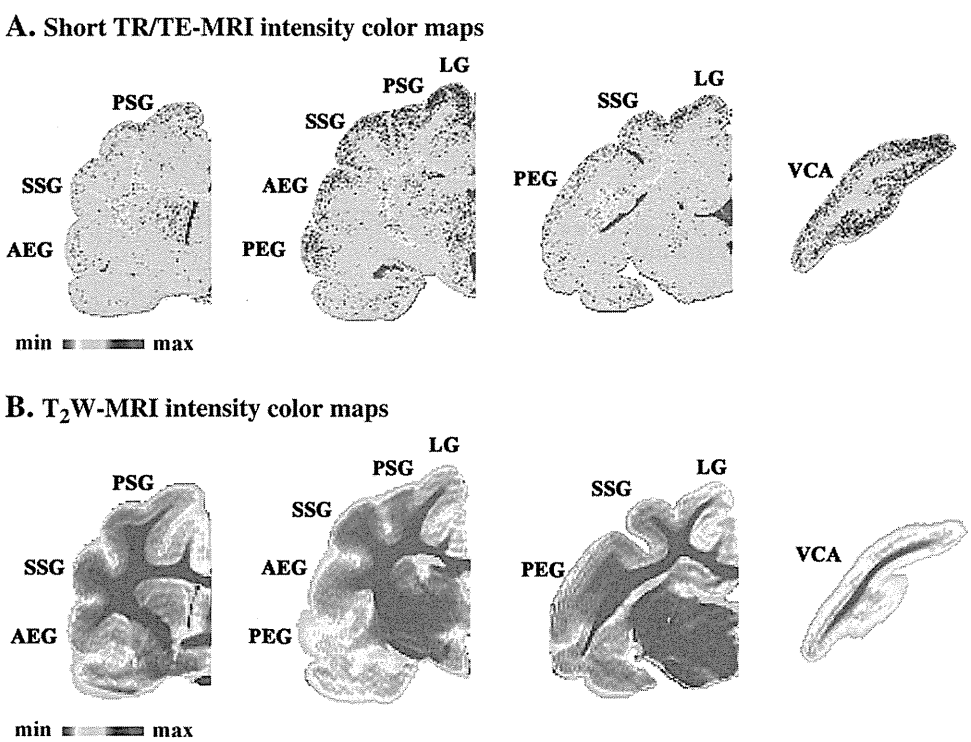

Fig. 5. Representative coronal images of short TR/TE (typical T_1-weighted parameter setting for conventional MRI) and T_2W (long TR/TE) MRI intensity color maps. (A) Short TR/TE-MRI intensity color maps of male ferret cerebrum. (B) T_2W-MRI intensity color maps of male ferret cerebrum. Signal intensities represented on short TR/TE- and T_2W-MRI images of each pixel were color-coded. The T_1W parameter setting (short TR/TE) did not show T_1-weighted contrast at the PFA-fixed brain sample under high-field MRI in the present study. Although shorter T_1 tissue, such as white matter, must be enhanced on T_1W-MRI, the signal was reduced due to the short T_2 of PFA medium (Supplement 1). AEG, anterior ectosylvian gyrus; LG, lateral gyrus; PEG, posterior ectosylvian gyrus; PSG, posterior sigmoid gyrus; SSG, suprasylvian gyrus; VCA, visual cortical area; PFA, paraformaldehyde.